

# An Adaptive Framework for Robust Structural Shape Optimization under Uncertainty

Oğuz Han Altıntaş <sup>\*</sup> Hamdullah Yücel <sup>†</sup>

February 6, 2026

## Abstract

This work proposes an adaptive framework to solve a robust structural shape optimization problem governed by linear elasticity models that account for uncertainties in the loading and material inputs. A posteriori error estimators are constructed to adjust the sample size, mesh size, and step length. The size of the sample set in the stochastic gradient approximation is dynamically determined depending on the variance of the shape derivative. When constructing the a posteriori error estimator in the physical domain, errors arising from the discretization of the deformation bilinear form, which provides a descent direction, are considered, in addition to errors from the discretization of the linear elasticity system. The step length in gradient-based optimization is also adaptively adjusted by estimating the Lipschitz constant of the stochastic shape derivative. Moreover, an analysis of the existence and distributed-form derivation of the stochastic shape derivative is provided. Finally, the proposed estimation-based adaptive stochastic optimization framework is validated on leg-like structural components, demonstrating its effectiveness in minimizing touchdown compliance under uncertain contact forces.

## 1 Introduction

Structural shape optimization is a powerful technique for enhancing complex scientific and engineering designs by optimizing material layout through variations in boundaries and connectivity within the design domain; see, e.g., [50, 54] for a comprehensive introduction. In many studies within the literature, input data such as loading conditions or material properties are typically assumed to be deterministic. However, due to factors like the manufacturing process, unknown loading conditions, variations in material properties, and lack of information, these problems inherently contain various types of uncertainties. These uncertainties may be related to loading, materials, geometry, or model-based factors [53]. Therefore, it is crucial to account for these uncertainties to ensure a robust and reliable design.

Over the last two decades, researchers have delved into shape and/or topology optimization problems that incorporate uncertainty. In works such as [1, 33], the methods like the worst-case approach and fuzzy techniques, which do not rely on statistical information about the uncertainty of the phenomenon, utilize a qualitative notion of its magnitude. The findings from these studies indicate that the resulting optimal designs often lead to poor structural performance. The methods that use statistical information represented by the statistical moments of the structural response (e.g., mean and variance) or the tails of probability distributions yield promising results. The former one is known as robust design optimization [11, 41, 56], which focuses on creating optimal designs that are less sensitive to variations in the input data. This type of risk is useful if one is focused on achieving good average performance and care little about variability. The latter approach is referred to as reliability-based design optimization [21, 39]. Such kind of risk-averse

---

<sup>\*</sup>Institute of Applied Mathematics, METU, Ankara, Türkiye, [oguz.altintas@metu.edu.tr](mailto:oguz.altintas@metu.edu.tr)

<sup>†</sup>Institute of Applied Mathematics, METU, Ankara, Türkiye, [yucelh@metu.edu.tr](mailto:yucelh@metu.edu.tr)

formulations focus on managing extreme or rare events to achieve a specified level of reliability using probabilistic constraints. However, this is beyond the scope of the present study. Instead, we mainly investigate a numerical approximation of the robust structural shape optimization problem formulated with a (risk-neutral) expectation measure, accounting for uncertainties in loading and material inputs within a linear elasticity model.

Compared to solving deterministic shape optimization problems, robust shape optimization problems pose more complex challenges due to the difficulty of discretizing both physical and stochastic domains. Up to now, a great deal of effort has been devoted to the development of efficient methods for solving PDEs with uncertain inputs, based on projection methods (e.g., polynomial chaos [61], and stochastic Galerkin (SG) [7]), and sampling methods (e.g., Monte Carlo [29], stochastic collocation [6]). In the projection approaches, one approximates the PDE solution by projecting it onto a given basis that is cheap to compute, whereas the sample-based approaches generate a finite set of realizations of the PDE solution that are then used to compute statistics or are interpolated to build an approximation of the full solution. In the realm of the robust structural shape and topology optimization, we refer to [41] for the stochastic collocation method, [56] for the stochastic Galerkin approach, [2] for the perturbation methods, and [23] for the Monte Carlo technique. There are other studies on the robust shape optimization problem, such as [20] that uses a two-stage stochastic programming algorithm, [45] that utilizes an approach based on a dimension-adaptive sparse grid, and [5] that is based on a non-intrusive approach based on the anchored ANOVA Petrov-Galerkin projection scheme. Although the polynomial chaos or SC methods, generally, exhibit better convergence behaviour for low dimensional uncertainties, a larger number of stochastic dimensions due to the low regularity of random fields may cause a prohibitively large algebraic system, called as the curse of dimensionality. Therefore, we concentrate on Monte Carlo sampling methods (more generally, sample average approximation), which allow us to effectively represent the stochastic problem as a finite summation, even when dealing with a large number of uncertainties.

Optimization problems with uncertainty governed by PDEs have been studied by using deterministic optimization methods in combination with sampling or discretization schemes in the stochastic space. However, using a gradient descent approach requires solving  $2N$  PDEs (i.e.,  $N$  state and  $N$  adjoint state equations) at each iteration: a cost that is rarely affordable. To reduce computational complexity, there have been several contributions to stochastic optimization but they are limited; see, e.g., [32, 34, 44, 57] for PDE-constrained optimization problems and [24, 36] for shape optimization problems. For the stochastic optimization problems, it is well-known that the variance of the quantity of interest (QoI) is inversely proportional to the number of samples  $N$  and thus a large sample size will lead to a high probability of an optimal solution for the QoI. However, using a large sample size at each optimization iteration is unnecessarily costly with respect to the number of samples. For this reason, it will be useful to use an adaptive sampling strategy as discussed in [12, 15] to keep sample size as small as possible. In this methodology, a relatively small sample size is chosen at the beginning, and if the process is likely to produce improvement in the QoI, the sample size remains unchanged. Otherwise, a larger sample size is selected according to an *a posteriori* error indicator related to the variance of the sampled QoI. One of the gains of this process is that it provides a rapid progress in the early stages with the usage of a small initial sample size, whereas a larger sample size yields high accuracy in the solution as needed. For each sample it is also essential to account for errors stemming from the approximation of the domain and the solution of the PDE constraint, as well as their derivatives within the finite elements. To minimize computational complexity while preserving high accuracy in the geometric description of the optimal design and the approximation of the objective functional, it is crucial to keep the degrees of freedom (DoF) as low as possible and to ensure that the shape gradient is strictly negative along the specified descent direction. To address these concerns, *a posteriori* error estimators can provide valuable insights during the optimization process. Several works in the literature have highlighted the considerable potential of *a posteriori* error estimators in achieving optimal designs for shape and topology optimization challenges. The Zienkiewicz–Zhu error estimator was employed in [9] to improve the accuracy of solutions arising from the approximation of the underlying differential problem, while utilizing the norm of the design gradient of

the Lagrange function as an a posteriori error estimator for optimality conditions. This research was later extended through the dual-weighted residual method to control the PDE error, while the Laplace–Beltrami error indicator was adopted to account for geometric errors associated with domain deformations in [46]. Furthermore, we refer to [14, 47, 51] for the application of adaptive mesh refinement in the shape/topology optimization problems.

The principal contribution of this work lies in the development of an efficient adaptive framework for solving robust structural shape optimization problems governed by a linear elasticity model that incorporates uncertainties in both loading and material parameters. The proposed approach not only determines the size of the sample set in an adaptive manner, but also employs a posteriori error estimators based on the dual-weighted residual (DWR) method [10] to enhance the efficiency of the finite element analysis, thereby improving the numerical solution beyond what can be achieved through fixed mesh refinement. In constructing the a posteriori error estimator, errors arising from the discretization of the deformation bilinear form, which provides a descent direction, are taken into account in addition to those resulting from the discretization of the constraint PDE, namely the linear elasticity system. Furthermore, during the mesh deformation process guided by the descent direction, the step length within the gradient-based optimization procedure is adaptively adjusted by estimating the Lipschitz constant, ensuring stable and efficient convergence.

The remainder of this paper is organized as follows. In Section 2, we introduce the linear elasticity problem formulated as a PDE constraint, together with the compliance objective functional subject to a volume fraction constraint, under suitable assumptions and notation. The existence and derivation of the shape derivative associated with the expected compliance minimization problem, subject to a penalized volume constraint, are presented in Section 3. Section 4 discusses the numerical techniques used to discretize the infinite-dimensional optimization problem, thereby yielding its finite-dimensional approximation, and describes the corresponding optimization procedures. In addition, the a posteriori error estimators used to adaptively control the sample size, mesh refinement, and optimization step length are introduced. Section 5 then presents the proposed adaptive algorithm, which incorporates the dual-weighted residual (DWR) method for multiple goal functionals and dynamically updates the sample size. To demonstrate the effectiveness and robustness of the proposed estimation-based adaptive stochastic optimization framework, Section 6 presents a set of numerical experiments for a benchmark compliance minimization problem with randomly generated input data. The focus is on the shape optimization of leg-like structural components, with the objective of minimizing compliance at touchdown under uncertain contact force conditions. The performance of the algorithm is examined in three settings: (i) a randomness study conducted on a fixed mesh, (ii) a mesh refinement study using full Monte Carlo sampling, and (iii) a fully adaptive framework that combines both adaptive sampling and adaptive mesh refinement. Finally, concluding remarks and potential directions for future research are discussed in Section 7.

## 2 Model problem

Throughout this paper, we adhere to the conventional notation for Sobolev spaces  $W^{m,p}(\mathcal{D})$  with  $m \geq 0$  and  $1 \leq p \leq \infty$ , as outlined in standard references such as [13, 19], equipped with the norm  $\|\cdot\|_{m,p,\mathcal{D}}$  and the seminorm  $|\cdot|_{m,p,\mathcal{D}}$  on an open and bounded polygonal physical domain  $\mathcal{D} \subset \mathbb{R}^2$ , with Lipschitz boundary  $\partial\mathcal{D}$ . In particular, we denote  $W^{m,2}(\mathcal{D})$  by  $H^m(\mathcal{D})$  and the corresponding norm and semi-norm by  $\|\cdot\|_{m,\mathcal{D}}$  and  $|\cdot|_{m,\mathcal{D}}$ , respectively. The space of square integrable functions over  $\mathcal{D}$  is represented by  $L^2(\mathcal{D})$  endowed with the norm  $\|\cdot\|_{\mathcal{D}}$  and inner products on  $L^2(\mathcal{D})$  and  $L^2(\partial\mathcal{D})$  are denoted by  $(\cdot, \cdot)_{\mathcal{D}}$  and  $(\cdot, \cdot)_{\partial\mathcal{D}}$ , respectively.  $C^k(\mathbb{R}^2, \mathbb{R}^2)$  is the set of  $k$ -times continuously differentiable vector-valued functions and  $C > 0$  is a generic constant independent of any discretization parameters. A complete probability space is denoted by  $(\Omega, \mathfrak{F}, \mathbb{P})$ , where  $\Omega$  represents the set of all possible outcomes  $\omega \in \Omega$ ,  $\mathfrak{F}$  is a  $\sigma$ -algebra of measurable events, and  $\mathbb{P} : \mathfrak{F} \rightarrow [0, 1]$  denotes the associated probability measure. For a random variable  $v : \Omega \rightarrow H^k(\mathcal{D})$ ,

the Bochner space  $L^p(\Omega; H^k(\mathcal{D}))$  is then defined as

$$L^p(\Omega; H^k(\mathcal{D})) := \left\{ v : \Omega \rightarrow H^k(\mathcal{D}) : v \text{ is strongly measurable,} \right. \\ \left. \|v\|_{L^p(\Omega; H^k(\mathcal{D}))} < \infty \right\},$$

where

$$\|v\|_{L^p(\Omega; H^k(\mathcal{D}))} = \begin{cases} \left( \int_{\Omega} \|v(\omega)\|_{k, \mathcal{D}}^p d\mathbb{P}(\omega) \right)^{1/p}, & \text{for } 1 \leq p < \infty, \\ \text{ess sup}_{\omega \in \Omega} \|v(\omega)\|_{k, \mathcal{D}}, & \text{for } p = \infty. \end{cases}$$

Additionally, the isomorphism relation, that is,  $H^k(\mathcal{D}) \otimes L^p(\Omega) \simeq L^p(\Omega; H^k(\mathcal{D})) \simeq H^k(\mathcal{D}; L^p(\Omega))$  holds; see, [7] for more details. Further, for a real-valued random field  $\varkappa : \mathcal{D} \times \Omega \rightarrow \mathbb{R}$  within the probability space  $(\Omega, \mathfrak{F}, \mathbb{P})$ , the expected value (also known as the mean) and the covariance are provided, respectively, by

$$\mathbb{E}[\varkappa](x) := \int_{\Omega} \varkappa(x, \omega) d\mathbb{P}(\omega), \quad x \in \mathcal{D}, \\ \mathcal{C}_{\varkappa}(x, \tilde{x}) := \int_{\Omega} (\varkappa(x, \omega) - \mathbb{E}[\varkappa](x))(\varkappa(\tilde{x}, \omega) - \mathbb{E}[\varkappa](\tilde{x})) d\mathbb{P}(\omega), \quad x, \tilde{x} \in \mathcal{D}.$$

By setting  $\tilde{x} = x$ , one obtains the variance  $\mathcal{V}_{\varkappa}(x) = \mathcal{C}_{\varkappa}(x, x)$  and the corresponding standard deviation  $\kappa_{\varkappa}(x) = \sqrt{\mathcal{V}_{\varkappa}(x)}$ .

## 2.1 PDE constraint: linear elasticity

A linearized elasticity system that incorporates uncertainties in both the loading and material parameters within the domain  $\mathcal{W} \subset \mathbb{R}^2$  is formulated as follows

$$-\operatorname{div}(A(x, \omega) \nabla^s u(x, \omega)) = f(x, \omega) \quad \text{in } \mathcal{W} \times \Omega, \quad (1a)$$

$$u(x, \omega) = 0 \quad \text{on } \Gamma_d \times \Omega, \quad (1b)$$

$$(A(x, \omega) \nabla^s u(x, \omega))n = g(x, \omega) \quad \text{on } \Gamma_n \times \Omega, \quad (1c)$$

$$(A(x, \omega) \nabla^s u(x, \omega))n = 0 \quad \text{on } \Gamma_f \times \Omega, \quad (1d)$$

where  $\Gamma_d$  and  $\Gamma_n$  are fixed, disjoint subsets of the boundary  $\partial\mathcal{W}$ , representing the Dirichlet and Neumann boundaries, respectively. The remaining portion of the boundary,

$$\Gamma_f := \partial\mathcal{W} \setminus (\Gamma_d \cup \Gamma_n),$$

denotes the *free boundary*, which is the only part subject to optimization during the shape update process. Here,  $f : \mathcal{W} \times \Omega \rightarrow \mathbb{R}^2$  is the body force,  $g : \Gamma_n \times \Omega \rightarrow \mathbb{R}^2$  is the traction (Neumann loading) force,  $u : \mathcal{W} \times \Omega \rightarrow \mathbb{R}^2$  denotes the displacement field,  $\nabla^s u = \frac{1}{2}(\nabla u^{\top} + \nabla u) : \mathcal{W} \times \Omega \rightarrow \mathbb{R}^{2 \times 2}$  is the symmetric strain tensor field,  $A$  represents the Hooke elasticity tensor,  $A \nabla^s u : \mathcal{W} \times \Omega \rightarrow \mathbb{R}^{2 \times 2}$  is the stress tensor field, and  $n$  denotes the unit outward normal vector to  $\partial\mathcal{W}$ . Further, we note that the divergence operator,  $\operatorname{div}$ , and the gradient operator,  $\nabla$ , always refer to differentiation with respect to the spatial variable  $x$ , unless otherwise stated.

In the optimization process, handling the variable domain  $\mathcal{W}$  poses significant computational challenges. To circumvent these difficulties, the computational problem is reformulated on a fixed reference domain  $\mathcal{D}$  by employing the *ersatz material* approach [3, 58]. In this framework, the strong (solid) material phase is distinguished from the void (or weak) phase material by defining the Hooke elasticity tensor as

$$A_{\mathcal{W}} = A \chi_{\mathcal{W}} + \epsilon A \chi_{\mathcal{D} \setminus \mathcal{W}}, \quad (2)$$

where  $\epsilon$  is a prescribed small parameter satisfying  $0 < \epsilon \ll 1$ , and  $\chi_{\mathcal{W}}$  denotes the characteristic (indicator) function of the domain  $\mathcal{W}$ . Here,  $A$  lays in the strong phase  $\mathcal{W} \subset \mathcal{D}$ , whereas  $\epsilon A$  stays

in the weak phase  $\mathcal{D} \setminus \mathcal{W}$ . For any symmetric matrix  $\zeta$ , Hooke's law for a linear isotropic elastic material is characterized by

$$A(x, \omega) \zeta = 2\mu(x, \omega) \zeta + \lambda(x, \omega) \operatorname{tr}(\zeta) \mathbf{Id},$$

where  $\mu, \lambda \in \mathbb{R}$  are the Lamé moduli of the material, which are assumed to depend on both  $x \in \mathcal{W}$  and  $\omega \in \Omega$ ,  $\operatorname{tr}(\cdot)$  denotes the trace operator, and  $\mathbf{Id}$  is the  $2 \times 2$  identity matrix. In the application of the ersatz material approach, the optimization process is still performed with respect to the variable set  $\mathcal{W}$ , which is embedded within the fixed, larger computational domain  $\mathcal{D}$ . Accordingly, the linear elasticity system is reformulated as

$$-\operatorname{div}(A_{\mathcal{W}}(x, \omega) \nabla^s u(x, \omega)) = f_{\mathcal{W}}(x, \omega) \quad \text{in } \mathcal{D} \times \Omega, \quad (3a)$$

$$u(x, \omega) = 0 \quad \text{on } \Gamma_d \times \Omega, \quad (3b)$$

$$(A_{\mathcal{W}}(x, \omega) \nabla^s u(x, \omega)) n = g(x, \omega) \quad \text{on } \Gamma_n \times \Omega, \quad (3c)$$

$$(A_{\mathcal{W}}(x, \omega) \nabla^s u(x, \omega)) n = 0 \quad \text{on } \Gamma_f \times \Omega, \quad (3d)$$

where  $\partial\mathcal{D} = \bar{\Gamma}_d \cup \bar{\Gamma}_n \cup \bar{\Gamma}_f$  and the interface between the strong and weak material phases is given by  $\partial\mathcal{W}$ , which constitutes the only free (i.e., design-dependent) interface. For sufficiently small values of  $\epsilon$ , the solution of (3) corresponds to an approximation of the solution to (1); see also [22] for discussions on stability and numerical consistency issues.

To ensure the regularity of the displacement solution  $u : \mathcal{D} \times \Omega \rightarrow \mathbb{R}^2$  in (3), we require the following assumptions on the given random inputs.

**Assumption 1.** *Let the Lamé parameters  $\lambda(x, \omega)$  and  $\mu(x, \omega)$  belong to  $L^\infty(\Omega; L^\infty(\mathcal{D}))$ . There exist positive constants  $\mu_{\min}, \mu_{\max}, \lambda_{\min}, \lambda_{\max} \in (0, \infty)$  such that*

$$\mu_{\min} \leq \mu(x, \omega) \leq \mu_{\max} \quad \text{and} \quad \lambda_{\min} \leq 2\mu(x, \omega) + 2\lambda(x, \omega) \leq \lambda_{\max}$$

for almost every  $(x, \omega) \in \mathcal{D} \times \Omega$ .

**Assumption 2.** *The stochastic body force  $f_{\mathcal{W}}(x, \omega)$  and boundary traction  $g(x, \omega)$  possess continuous and bounded covariance functions, and satisfy*

$$f_{\mathcal{W}} \in L^2(\Omega; L^2(\mathcal{D})^2) \quad \text{and} \quad g \in L^2(\Omega; L^2(\Gamma_n)^2).$$

Then, introducing the Hilbert space  $H_d^1(\mathcal{D})^2 := \{v \in H^1(\mathcal{D})^2 : v = 0 \text{ on } \Gamma_d\}$  equipped with  $H^1(\mathcal{D})^2$ -norm, we state the weak formulation of the elasticity problem (3) as follows: Find  $u \in L^2(\Omega; H_d^1(\mathcal{D})^2)$  such that

$$a[u, v] = [f_{\mathcal{W}}, v] + [g, v]_{\Gamma_n} \quad \forall v \in L^2(\Omega; H_d^1(\mathcal{D})^2), \quad (4)$$

where

$$a[u, v] := \int_{\Omega} \int_{\mathcal{D}} A_{\mathcal{W}}(x, \omega) \nabla^s u(x, \omega) : \nabla^s v(x, \omega) dx d\mathbb{P}(\omega),$$

$$[f_{\mathcal{W}}, v] := \int_{\Omega} \int_{\mathcal{D}} f_{\mathcal{W}}(x, \omega) \cdot v(x, \omega) dx d\mathbb{P}(\omega),$$

$$[g, v]_{\Gamma_n} := \int_{\Omega} \int_{\Gamma_n} g(x, \omega) \cdot v(x, \omega) ds d\mathbb{P}(\omega),$$

where the notation  $:$  represents the Frobenius inner product of tensors. Given the assumptions outlined in Assumptions 1 and 2, the Lax-Milgram theorem allows us to assert that the problem described by (3) is well-posed; see, e.g., [45].

## 2.2 Objective functional: compliance

In this study, we address a robust structural shape optimization problem that accounts for uncertainties in both the loading and material parameters. The problem is formulated as

$$\min_{\mathcal{W} \in \mathcal{U}^{\text{ad}}} \mathbb{E}[J(\mathcal{W}, \omega)] \quad \text{subject to} \quad (3), \quad (5)$$

where  $J : \mathcal{U}^{\text{ad}} \times \Omega \rightarrow \mathbb{R}$  denotes the objective functional, such that the mapping  $\omega \mapsto J(\mathcal{W}, \omega)$  is  $\mathbb{P}$ -integrable and well-defined for all admissible domains  $\mathcal{W} \in \mathcal{U}^{\text{ad}} \subset \mathcal{D}$ . Here,  $\mathcal{U}^{\text{ad}}$  represents the set of admissible shapes.

Before discussing the objective functional and the set of admissible shapes in (5), we recall the notion of the  $\varepsilon$ -cone property [17].

**Definition 1** ( $\varepsilon$ -cone property). *An open set  $\mathcal{W} \subset \mathbb{R}^2$  is said to satisfy the  $\varepsilon$ -cone property if, for every point  $x \in \partial\mathcal{W}$ , there exists a unit vector  $q \in \mathbb{R}^2$  with  $|q| = 1$  such that*

$$\mathcal{C}(y, q, \varepsilon) \subset \mathcal{W} \quad \forall y \in \overline{\mathcal{W}} \cap B(x, \varepsilon),$$

where the open cone  $\mathcal{C}(y, q, \varepsilon)$  is defined by

$$\mathcal{C}(y, q, \varepsilon) = \left\{ z \in \mathbb{R}^2 : (z - y, q) \geq |z - y| \cos \varepsilon, 0 < |z - y| < \varepsilon \right\}.$$

We now define the class of admissible domains  $\mathcal{U}^{\text{ad}}$  as

$$\mathcal{U}^{\text{ad}} = \{\mathcal{W} \in \mathcal{W}_\varepsilon : \Gamma_d \cup \Gamma_n \subset \partial\mathcal{W}, 0 < |\mathcal{W}| = \varsigma |\mathcal{D}| \}, \quad (6)$$

where  $\mathcal{W}_\varepsilon := \{\mathcal{W} \subset \mathcal{D} \text{ open} : \mathcal{W} \text{ satisfies the } \varepsilon\text{-cone property}\}$ , and  $\varsigma \in (0, 1)$  denotes the pre-scribed volume fraction, that is, the ratio between the domain volume  $|\mathcal{W}| = \int_{\mathcal{W}} dx$  and the working domain volume  $|\mathcal{D}|$ .

For a given domain  $\mathcal{W} \in \mathcal{U}^{\text{ad}}$  and each realization  $\omega \in \Omega$ , we define the objective functional  $J$  in (5) as the commonly recognized output functional, namely, *compliance*

$$J(\mathcal{W}, \omega) = \int_{\mathcal{D}} f_{\mathcal{W}}(x, \omega) \cdot u(x, \omega) dx + \int_{\Gamma_n} g(x, \omega) \cdot u(x, \omega) ds, \quad (7)$$

where  $u(x, \omega)$  denotes the weak solution of the elasticity system (3) corresponding to the realization  $\omega \in \Omega$ . Accordingly, the robust shape optimization problem is formulated as

$$\mathcal{W}^* = \arg \min_{\mathcal{W} \in \mathcal{U}^{\text{ad}}} \mathcal{J}(\mathcal{W}) := \mathbb{E}[J(\mathcal{W}, \omega)]. \quad (8)$$

Under the  $\varepsilon$ -cone assumption on the admissible design set  $\mathcal{U}^{\text{ad}}$ , the existence of a solution to the optimization problem (8) can be established; see, for instance, [45, Theorem 2.1]. To enforce the volume constraint in practice, a penalization approach is employed, leading to the following formulation:

$$\min_{\mathcal{W} \in \mathcal{D}} \mathcal{J}^P(\mathcal{W}) = \mathbb{E}[J^P(\mathcal{W}, \omega)], \quad (9)$$

where the penalized objective functional is defined as

$$J^P(\mathcal{W}, \omega) = J(\mathcal{W}, \omega) + \frac{\Lambda}{2} \left( \varsigma - \frac{|\mathcal{W}|}{|\mathcal{D}|} \right)^2, \quad (10)$$

with  $\Lambda > 0$  denoting the penalty parameter.

### 3 Stochastic shape derivative

In the gradient-based minimization of objective functions, we follow the classical notion of Hadamard's boundary variation method (see, e.g., [54]) for defining perturbed shapes from the smooth initial shape  $\mathcal{W}_0 \in \mathcal{U}^{\text{ad}}$ .

Let  $\text{Id}$  be the identity map on the space  $W^{1,\infty}(\mathbb{R}^2)$  and consider a vector field  $\theta \in W^{1,\infty}(\mathbb{R}^2)$  (also called the *deformation vector*). Then, the perturbed domain becomes

$$\mathcal{W}_t = (\text{Id} + \theta)(\mathcal{W}),$$

for each vector-valued function  $\dot{x}(t) = \theta(x(t))$ , with initial condition  $x(0) = x_0$  and the associated flow  $\Phi_t : \mathbb{R}^2 \rightarrow \mathbb{R}^2$  defined for each  $x_0 \in \mathbb{R}^2$  as  $\Phi_t(x_0) = x(t)$ , where  $x : [0, \tau] \rightarrow \mathbb{R}^d$  and  $t \in [0, \tau]$ . Furthermore, the mapping  $\text{Id} + \theta$  is a diffeomorphism in  $\mathbb{R}^d$  for sufficiently small  $\theta$ , so that  $\mathcal{W}_t \subset \overline{\mathcal{D}}$ ; see [54, Theorem 2.16].

Now we are ready to introduce the definition of the shape derivative for a fixed realization  $\omega \in \Omega$ .

**Definition 2.** Let  $\mathcal{D} \subset \mathbb{R}^2$  be open and  $\omega \in \Omega$  be fixed. Then, the Eulerian semiderivative of a functional  $J(\cdot, \omega)$  at  $\mathcal{W} \subset \mathcal{D}$  with  $|\mathcal{W}| \neq 0$  in the direction  $\theta \in C_0^k(\mathcal{D}, \mathbb{R}^d)$ ,  $k \in \mathbb{N}$  is defined, whenever the limit exists, by

$$dJ(\mathcal{W}, \omega)(\theta) = \lim_{t \rightarrow 0^+} \frac{J(\Phi_t(\mathcal{W}), \omega) - J(\mathcal{W}, \omega)}{t}.$$

If for every direction  $\theta \in C_0^\infty(\mathcal{D}, \mathbb{R}^2)$ , the derivative exists and the mapping  $\theta \mapsto dJ(\mathcal{W}, \omega)(\theta) : C_0^\infty(\mathcal{D}, \mathbb{R}^2) \rightarrow \mathbb{R}$  is linear and continuous, then the functional  $J(\cdot, \omega)$  is said to be shape differentiable.

Under the above definition, the objective function in (9), that is,  $\mathcal{J}^P(\mathcal{W}) = \mathbb{E}[J^P(\mathcal{W}, \omega)]$ , is shape differentiable in  $\mathcal{W}$  provided that  $J^P(\cdot, \omega)$  is shape differentiable in  $\mathcal{W}$  for almost every  $\omega \in \Omega$ . In this case, the derivative satisfies

$$d\mathcal{J}^P(\mathcal{W})(\theta) = \mathbb{E}[dJ^P(\mathcal{W}, \omega)(\theta)], \quad \forall \theta \in C_0^\infty(\mathcal{D}, \mathbb{R}^2),$$

see, for instance, [31, Lemma 2.14].

Next, we compute the shape derivative of the expression in (10), that is,  $J^P(\mathcal{W}, \omega)$  by employing the averaged adjoint method and Lagrangian-type method introduced in [55] for a fixed but arbitrary realization  $\omega \in \Omega$ .

**Proposition 1.** For a fixed realization  $\omega \in \Omega$ , the shape derivative of the penalized cost functional  $J^P(\mathcal{W}, \omega)$  in (10) is given by

$$dJ^P(\mathcal{W}, \omega)(\theta) = \underbrace{\int_{\mathcal{D}} (S_\omega : \nabla \theta + T_\omega \cdot \theta) dx}_{dJ(\mathcal{W}, \omega)(\theta)} - \tilde{\Lambda} \int_{\mathcal{W}} \operatorname{div} \theta dx, \quad (11)$$

where

$$\begin{aligned} S_\omega &:= 2\nabla u(\cdot, \omega)^\top A_{\mathcal{W}} \nabla^s u(\cdot, \omega) + (2f_{\mathcal{W}} \cdot u(\cdot, \omega) - A_{\mathcal{W}} \nabla^s u(\cdot, \omega) : \nabla^s u(\cdot, \omega)) \text{Id}, \\ T_\omega &:= 2(\nabla f_{\mathcal{W}} u(\cdot, \omega) + f_{\mathcal{W}}^\top \nabla u(\cdot, \omega)), \\ \tilde{\Lambda} &:= \frac{\Lambda}{|\mathcal{D}|} \left( \varsigma - \frac{|\mathcal{W}|}{|\mathcal{D}|} \right), \end{aligned}$$

and  $u(\cdot, \omega)$  denotes the weak solution of (3) posed in the spatial domain  $\mathcal{W}$  for almost every  $\omega \in \Omega$ .

*Proof* Let  $\mathcal{W}_t = \Phi_t(\mathcal{W}) \subset \mathcal{D}$  be a parametrized domain, where it is assumed that  $\Phi_t = \text{Id}$  on the boundary  $\Gamma_d \cup \Gamma_n$ . Further, let  $u_t(\omega) \in H_d^1(\mathcal{D})^2$  be the weak solution of (3) with  $\mathcal{W}$

substituted by  $\mathcal{W}_t$ . To facilitate the differentiation with respect to  $t$ , we perform a change of variables  $x \rightarrow \Phi_t(x)$ , thereby obtaining an expression that depends on  $A_{\mathcal{W}}$  and  $f_{\mathcal{W}}$  instead of  $A_{\mathcal{W}_t}$  and  $f_{\mathcal{W}_t}$ . An application of the chain rule to  $u^t := u_t \circ \Phi_t$  yields

$$\nabla u^t = \nabla(u_t \circ \Phi_t) = (\nabla u_t) \circ \Phi_t \nabla \Phi_t,$$

and we define

$$\varepsilon(t, u^t) := \nabla^s u_t \circ \Phi_t = \frac{1}{2} \left( \nabla u^t \nabla \Phi_t^{-1} + (\nabla u^t \nabla \Phi_t^{-1})^\top \right). \quad (12)$$

Now, we follow the formal Lagrange method and define the Lagrangian  $\mathcal{L} : [0, \tau] \times H_d^1(\mathcal{D})^2 \times H_d^1(\mathcal{D})^2 \rightarrow \mathbb{R}$  in view of (12),

$$\begin{aligned} \mathcal{L}(t, v, q; \omega) = & \int_{\mathcal{D}} f_{\mathcal{W}}(\omega) \cdot v \zeta(t) dx + \int_{\Gamma_n} g(\omega) \cdot v ds \\ & + \int_{\mathcal{D}} (A_{\mathcal{W}}(\omega) \varepsilon(t, v) : \varepsilon(t, q) - f_{\mathcal{W}}(\omega) \cdot q) \zeta(t) dx \\ & - \int_{\Gamma_n} g(\omega) \cdot q ds - \int_{\Gamma_d} q \cdot A_{\mathcal{W}}(\omega) \varepsilon(0, v) n ds \\ & - \int_{\Gamma_d} v \cdot A_{\mathcal{W}}(\omega) \varepsilon(0, q) n ds, \end{aligned} \quad (13)$$

where  $\zeta(t)$  is the Jacobian of the transformation  $x \rightarrow \Phi_t(x)$  and  $\varepsilon(0, v) = \nabla^s v$ . Note that the Jacobian  $\zeta(t)$  and the mapping  $\Phi_t$  do not appear in the boundary integrals since  $\Phi_t = \text{Id}$  is assumed on  $\Gamma_d \cup \Gamma_n$ .

One can easily see that  $J(\mathcal{W}_t, \omega) = \mathcal{L}(t, u^t, q; \omega)$  for all  $q \in H_d^1(\mathcal{D})^2$ . The corresponding shape derivative is then computed by employing

$$dJ(\mathcal{W}, \omega)(\theta) = \frac{d}{dt} \mathcal{L}(t, u^t, z; \omega)|_{t=0} = \partial_t \mathcal{L}(0, u^0, z; \omega), \quad (14)$$

in which we can elide the computation steps related to  $u^t$ . In (14), the adjoint variable  $z$  is determined from the first-order optimality condition  $\partial_v \mathcal{L}(0, u, z; \omega)(\varphi) = 0 \ \forall \varphi \in H_d^1(\mathcal{D})^2$ . By using the symmetry property  $A_{\mathcal{W}} = A_{\mathcal{W}}^\top$  for each  $\omega \in \Omega$  and noting that  $\zeta(0) = 1$ , (13) yields

$$\begin{aligned} (\delta_v \mathcal{L}, \varphi)|_{0, u, z} = & \int_{\mathcal{D}} f_{\mathcal{W}}(\omega) \cdot \varphi dx + \int_{\Gamma_n} g(\omega) \cdot \varphi ds \\ & + \int_{\mathcal{D}} (A_{\mathcal{W}}(\omega) \varepsilon(0, \varphi) : \varepsilon(0, z)) dx \\ & - \int_{\Gamma_d} z \cdot A_{\mathcal{W}}(\omega) \varepsilon(0, \varphi) n ds - \int_{\Gamma_d} \varphi \cdot A_{\mathcal{W}}(\omega) \varepsilon(0, z) n ds, \end{aligned} \quad (15)$$

for all  $\varphi \in H_d^1(\mathcal{D})^2$ . Here,  $\delta_v$  denotes the directional derivative in the direction of  $v$ . Applying integration by parts to (15) yields the following strong form of the adjoint  $z(\omega) \in H^2(\mathcal{D})^2$  for almost every  $\omega \in \Omega$ :

$$-\operatorname{div}(A_{\mathcal{W}}(x, \omega) \nabla^s z) = -f_{\mathcal{W}}(x, \omega) \quad \text{in } \mathcal{D}, \quad (16a)$$

$$z = 0 \quad \text{on } \Gamma_d, \quad (16b)$$

$$(A_{\mathcal{W}}(x, \omega) \nabla^s z) n = -g(x, \omega) \quad \text{on } \Gamma_n, \quad (16c)$$

$$(A_{\mathcal{W}}(x, \omega) \nabla^s z) n = 0 \quad \text{on } \Gamma_f. \quad (16d)$$

Next, the shape derivative from (13) can be computed as follows

$$\begin{aligned}
dJ(\mathcal{W}, \omega)(\theta) &= \partial_t \mathcal{L}(0, u, z; \omega) \\
&= \int_{\mathcal{D}} (\partial_t (f_{\mathcal{W}}(\omega) \cdot u) \zeta(0) + (f_{\mathcal{W}}(\omega) \cdot u) \zeta'(0)) dx \\
&\quad + \int_{\mathcal{D}} \left( (A_{\mathcal{W}}(\omega) \partial_t \varepsilon(0, u) : \varepsilon(0, z) + A_{\mathcal{W}}(\omega) \varepsilon(0, u) : \partial_t \varepsilon(0, z)) \zeta(0) \right. \\
&\quad \left. + (A_{\mathcal{W}}(\omega) \varepsilon(0, u) : \varepsilon(0, z)) \zeta'(0) \right) dx \\
&\quad - \int_{\mathcal{D}} (\partial_t (f_{\mathcal{W}}(\omega) \cdot z) \zeta(0) + (f_{\mathcal{W}}(\omega) \cdot z) \zeta'(0)) dx.
\end{aligned} \tag{17}$$

Recalling that  $\zeta(0) = 1$ ,  $\zeta'(0) = \operatorname{div} \theta$ , and  $\dot{x}(t) = \theta$ , an application of the chain rule yields

$$\begin{aligned}
\partial_t \varepsilon(0, u) &= -\frac{1}{2} \left( \nabla u \nabla \theta + (\nabla u \nabla \theta)^\top \right), \\
\partial_t (f_{\mathcal{W}} \cdot u) &= (\nabla f_{\mathcal{W}} u + f_{\mathcal{W}}^\top \nabla u) \cdot \theta, \\
\partial_t (g \cdot u) &= (\nabla g u + g^\top \nabla u) \cdot \theta.
\end{aligned} \tag{18}$$

Then, substituting (18) into (17), we obtain

$$\begin{aligned}
dJ(\mathcal{W}, \omega)(\theta) &= \int_{\mathcal{D}} (\nabla f_{\mathcal{W}}(\omega) u + f_{\mathcal{W}}^\top(\omega) \nabla u) \cdot \theta dx + \int_{\mathcal{D}} (f_{\mathcal{W}}(\omega) \cdot u) \operatorname{div} \theta dx \\
&\quad - \int_{\mathcal{D}} ((\nabla u^\top A_{\mathcal{W}}(\omega) \nabla^s z + \nabla u^\top (A_{\mathcal{W}}(\omega) \nabla^s z)^\top) : \nabla \theta) dx \\
&\quad + \int_{\mathcal{D}} A_{\mathcal{W}}(\omega) \nabla^s u : \nabla^s z \operatorname{div} \theta dx \\
&\quad - \int_{\mathcal{D}} ((\nabla f_{\mathcal{W}}(\omega) z + f_{\mathcal{W}}^\top(\omega) \nabla z) \cdot \theta + (f_{\mathcal{W}}(\omega) \cdot z) \operatorname{div} \theta) dx.
\end{aligned}$$

By employing the symmetry property  $(A_{\mathcal{W}} \nabla^s u)^\top = A_{\mathcal{W}} \nabla^s u$  and using the relation  $z = -u$  obtained from (1) and (16), we arrive at

$$\begin{aligned}
dJ(\mathcal{W}, \omega)(\theta) &= \int_{\mathcal{D}} (2 \nabla u^\top A_{\mathcal{W}}(\omega) \nabla^s u + (2 f_{\mathcal{W}}(\omega) \cdot u - A_{\mathcal{W}}(\omega) \nabla^s u : \nabla^s u) \operatorname{Id}) : \nabla \theta dx \\
&\quad + \int_{\mathcal{D}} 2 (\nabla f_{\mathcal{W}}(\omega) u + f_{\mathcal{W}}^\top(\omega) \nabla u) \cdot \theta dx
\end{aligned} \tag{19}$$

for all  $\theta \in W^{1,\infty}(\mathbb{R}^2)$ .

For the shape derivative of the second term in (10), we use the distributed expression of the shape derivative of the volume [25, Theorem 4.1], namely,

$$dV(\mathcal{W})(\theta) = \int_{\mathcal{W}} \operatorname{div} \theta dx, \quad \text{where } \mathcal{V} = \int_{\mathcal{W}} dx. \tag{20}$$

Finally, by exploiting the linearity of the mapping  $\theta \mapsto dJ^P(\mathcal{W}, \omega)(\theta)$ , the desired result follows directly from the combination of (19) and (20).  $\square$

**Remark 1.** The expression in (11) is commonly referred to as the distributed, volumetric, or domain representation of the shape derivative. Under standard regularity assumptions, the shape derivative depends only on the restriction of the normal component  $\theta \cdot n$  to the interface  $\partial\mathcal{W}$ ; for further details, see [25, pp. 480–481]. Although the boundary (Hadamard) form of the shape derivative is frequently employed in the development of level-set based numerical algorithms, we adopt the domain expression in (11), motivated by the favorable performance of volumetric formulations in combination with finite element discretization (see, e.g., [35]).

We now establish the shape differentiability of the functional  $\mathcal{J}^P(\mathcal{W}, \omega)$  in (9) by employing the techniques developed in [31, Theorem 3.6], where the Laplace equation is treated as the governing PDE constraint.

**Theorem 1.** *Let  $\partial\mathcal{W}$  be a  $C^2$ -boundary. Then, the functional  $\mathcal{J}^P(\mathcal{W}, \omega)$  in (9) is shape differentiable for all  $\mathcal{W} \in \mathcal{U}^{\text{ad}}$ .*

*Proof* Let  $u_t(\omega) \in H_d^1(\mathcal{D})^2$  be the weak solution of (3) with  $\mathcal{W}$  replaced by  $\mathcal{W}_t$ . According to [31, Lemma 2.14], to establish the shape differentiability of  $\mathcal{J}^P(\mathcal{W}, \omega)$ , it suffices to show that

$$\Psi_t(\omega) = \frac{\mathcal{J}^P(\mathcal{W}_t, \omega) - \mathcal{J}^P(\mathcal{W}, \omega)}{t} \leq C(\omega) \quad \forall t \in [0, \tau],$$

where  $C : \Omega \rightarrow \mathbb{R}$  is  $\mathbb{P}$ -integrable real function.

Applying the change of variables  $x \mapsto \Phi_t(x)$ , which allows the term  $f_{\mathcal{W}} = f_{\mathcal{W}_t} \circ \Phi_t$  to appear, we obtain

$$\begin{aligned} t\Psi_t(\omega) &= \int_{\mathcal{D}} f_{\mathcal{W}}(\omega) \cdot u^t(\omega) \zeta(t) dx - \int_{\mathcal{D}} f_{\mathcal{W}}(\omega) \cdot u(\omega) dx \\ &\quad + \int_{\Gamma_n} g(\omega) \cdot (u^t(\omega) - u(\omega)) ds \\ &\quad + \frac{\Lambda}{2} \left( \left( \varsigma - \frac{1}{|\mathcal{D}|} \int_{\mathcal{W}} \zeta(t) dx \right)^2 - \left( \varsigma - \frac{1}{|\mathcal{D}|} \int_{\mathcal{W}} dx \right)^2 \right), \end{aligned}$$

where  $u^t = u_t \circ \Phi_t$  and  $\zeta(t)$  denotes the Jacobian of the transformation  $x \mapsto \Phi_t(x)$ . From the boundedness of  $\zeta(t)$  for all  $t \in [0, \tau_1]$  [25, p. 256] and by applying the trace inequality, we obtain the following estimate

$$\begin{aligned} t\Psi_t(\omega) &\leq (C_{\zeta} \|f_{\mathcal{W}}(\omega)\|_{L^2(\mathcal{D})^2} + C_{tr} \|g(\omega)\|_{L^2(\Gamma_n)^2}) \|u^t(\omega) - u(\omega)\|_{L^2(\mathcal{D})^2} \\ &\quad + \frac{\Lambda}{2} \left( 2\varsigma - \frac{|\mathcal{W}|(1 + C_{\zeta})}{|\mathcal{D}|} \right) \frac{|\mathcal{W}|(1 - C_{\zeta})}{|\mathcal{D}|}. \end{aligned} \quad (21)$$

Next, we derive an upper bound for  $\|u^t(\omega) - u(\omega)\|_{L^2(\mathcal{D})^2}$ . Recall that  $u^t(\omega) = u_t(\omega) \circ \Phi_t$  satisfies the following variational formulation

$$\int_{\mathcal{D}} A_{\mathcal{W}}(\omega) \varepsilon(t, u^t) : \varepsilon(t, v) \zeta(t) dx = \int_{\mathcal{D}} f_{\mathcal{W}}(\omega) \cdot v \zeta(t) dx + \int_{\Gamma_n} g(\omega) \cdot v ds, \quad (22)$$

where  $v = v_t \circ \Phi_t$  and  $\varepsilon(t, \cdot) = \nabla^s(\cdot) \circ \Phi_t$ . Correspondingly, the associated energy functional  $\mathcal{E}_{\omega} : [0, \infty) \times H_d^1(\mathcal{D})^2 \rightarrow \mathbb{R}$  of (22) is defined by

$$\mathcal{E}_{\omega}(t, \varphi) = \frac{1}{2} \int_{\mathcal{D}} A_{\mathcal{W}}(\omega) |\varepsilon(t, \varphi)|^2 \zeta(t) dx - \int_{\mathcal{D}} f_{\mathcal{W}}(\omega) \cdot \varphi \zeta(t) dx - \int_{\Gamma_n} g(\omega) \cdot \varphi ds.$$

The first- and second-order Gâteaux derivatives of  $\mathcal{E}_{\omega}$  with respect to  $\varphi$  in the directions  $\psi, \psi_0 \in H^1(\mathcal{D})^2$  are given, respectively, by

$$\begin{aligned} (\delta_{\varphi} \mathcal{E}_{\omega}, \psi) &= \int_{\mathcal{D}} (A_{\mathcal{W}}(\omega) \varepsilon(t, \varphi) : \varepsilon(t, \psi) - f_{\mathcal{W}}(\omega) \cdot \psi) \zeta(t) dx - \int_{\Gamma_n} g(\omega) \cdot \psi ds, \\ (\delta_{\varphi}^2 \mathcal{E}_{\omega}, \psi, \psi_0) &= \int_{\mathcal{D}} A_{\mathcal{W}}(\omega) \varepsilon(t, \psi) : \varepsilon(t, \psi_0) \zeta(t) dx. \end{aligned}$$

An application of Assumption 1 together with the boundedness of  $\zeta(t)$  yields

$$(\delta_{\varphi}^2 \mathcal{E}_{\omega}, \psi, \psi) \geq c_1 \|\psi\|_{H^1(\mathcal{D})^2}^2, \quad (23)$$

which implies that the energy functional  $\mathcal{E}_\omega$  is strictly convex in  $H_d^1(\mathcal{D})^2$  with respect to  $\varphi$ . Consequently, the minimization problem

$$\min_{\varphi \in H_d^1(\mathcal{D})^2} \mathcal{E}_\omega(t, \varphi)$$

admits a unique solution for all  $t \in [0, \tau_2]$ , which solves for  $u^t(\omega)$  such that

$$(\delta_\varphi \mathcal{E}_\omega(t, u^t), \psi) = 0 \quad \forall \psi \in H_d^1(\mathcal{D})^2.$$

For  $u_r^t = ru + (1-r)u^t$  with  $r \in [0, 1]$ , it follows that

$$\begin{aligned} & \int_0^1 (\delta_\varphi^2 \mathcal{E}_\omega(t, u_r^t), u^t - u, u^t - u) \, dr \\ &= (\delta_\varphi \mathcal{E}_\omega(t, u), u^t - u) - (\delta_\varphi \mathcal{E}_\omega(t, u^t), u^t - u) \\ &= (\delta_\varphi \mathcal{E}_\omega(t, u), u^t - u) - (\delta_\varphi \mathcal{E}_\omega(0, u), u^t - u) \\ &= t (\delta_{t,\varphi} \mathcal{E}_\omega(t, u), u^t - u), \end{aligned}$$

where the mean value theorem is applied for the last inequality with  $r_t \in (0, 1)$ . By invoking Assumption 1 and using the continuous differentiability of  $\zeta(t)$  on  $[0, \tau_3]$ , we obtain the estimates

$$(\delta_{t,\varphi} \mathcal{E}_\omega(t, \varphi), \psi) \leq c_2 \|\varphi\|_{H^1(\mathcal{D})^2} \|\psi\|_{H^1(\mathcal{D})^2}. \quad (24)$$

Using (24) with (23), we get

$$\|u^t(\omega) - u(\omega)\|_{H^1(\mathcal{D})^2} \leq ct \|u(\omega)\|_{H^1(\mathcal{D})^2} \quad (25)$$

for all  $t \in [0, \min(\tau_2, \tau_3)]$ . Then, the stability result on the solution  $u^t(\omega)$  for any arbitrary  $\omega \in \Omega$  and (25) give us

$$\begin{aligned} \|u^t(\omega)\|_{H^1(\mathcal{D})^2} &\leq (ct + 1) \|u(\omega)\|_{H^1(\mathcal{D})^2}, \\ &\leq (ct + 1) C (\|f_{\mathcal{W}}(\omega)\|_{L^2(\mathcal{D})^2} + \|g(\omega)\|_{L^2(\Gamma_n)^2}) \end{aligned} \quad (26)$$

for all  $t \in [0, \tau_4]$ . Inserting (25) and (26) into (21) and using the Assumption 2, we obtain

$$\begin{aligned} t \Psi_t(\omega) &\leq (C_\zeta \|f_{\mathcal{W}}(\omega)\|_{L^2(\mathcal{D})^2} + \|g(\omega)\|_{L^2(\Gamma_n)^2}) (ct + 1) C \\ &\quad \times (\|f_{\mathcal{W}}(\omega)\|_{L^2(\mathcal{D})^2} + \|g(\omega)\|_{L^2(\Gamma_n)^2}) \\ &\quad + \frac{\Lambda}{2} \left( 2\zeta - \frac{|\mathcal{W}|(1 + C_\zeta)}{|\mathcal{D}|} \right) \frac{|\mathcal{W}|(1 - C_\zeta)}{|\mathcal{D}|} =: C(\omega) \end{aligned}$$

for all  $t \in [0, \tau]$  with  $\tau = \min\{\tau_1, \tau_2, \tau_3, \tau_4\}$ , which is the desired result.  $\square$

## 4 Numerical approximation techniques

In this section, we present numerical approximation techniques that reduce the infinite-dimensional optimization problem to a finite-dimensional one. To alleviate the computational burden caused by the number of samples and the degrees of freedom within the spatial domain, we introduce a posteriori error estimators for both settings. Additionally, the method for determining the descent direction for the shape derivative is explored and incorporated with the level-set method. Further, the step length in the (mini-batch) stochastic gradient method is adjusted adaptively by estimating the Lipschitz constant.

## 4.1 Representation of random fields

To obtain an approximate numerical solution to the problem described in (3), we utilize the finite dimensional noise assumption as introduced by Wiener in [59].

**Assumption 3.** *There exist an  $M$ -dimensional random vector  $\xi : \Omega \rightarrow \Xi = \prod_{i=1}^M \Gamma_i \subset \mathbb{R}^M$  with a joint density function of  $\rho(\xi) : \Xi \rightarrow \mathbb{R}_+^M$  such that  $z(\cdot, \omega) \equiv z_M(\cdot, \xi(\omega))$ , where  $z \in \{f_{\mathcal{W}}, g, \mu, \lambda\}$ .*

Assumption 3 can be realized through various finite-dimensional representation techniques for random fields. One common approach is to use a truncated Karhunen–Loève (KL) expansion [37, 42], given by

$$\varkappa_M(x, \omega) = \bar{\varkappa}(x) + \kappa_{\varkappa} \sum_{k=1}^M \sqrt{\lambda_k} b_k(x) \xi_k(\omega), \quad (27)$$

where  $\xi := \{\xi_k(\omega)\}_{k=1}^M$  are mutually uncorrelated random variables with zero mean and unit variance, i.e.,  $\mathbb{E}[\xi_k] = 0$  and  $\mathbb{E}[\xi_i \xi_j] = \delta_{i,j}$ . The functions  $\bar{\varkappa}(x)$  and  $\kappa_{\varkappa}$  denote the mean and standard deviation of the random field  $\varkappa$ , respectively. The eigenpairs  $\{\lambda_k, b_k\}_{k=1}^M$  are obtained by solving the Fredholm integral equation associated with the covariance kernel  $C_{\varkappa}$ , yielding a sequence of non-increasing positive eigenvalues  $\lambda_1 \geq \dots \geq \lambda_k \geq \dots > 0$  and mutually orthonormal eigenfunctions. To guarantee an analogue of Assumption 1, we further assume that  $\bar{\varkappa}(x) \geq \varkappa_{\min}$  for  $\varkappa \in \{\mu, \lambda\}$ .

## 4.2 Approximation in the parametric space

To approximate statistical moments, such as expected value or higher-order moments of a general quantity of interest like  $J^P(\mathcal{W}, \omega)$  in (10), we use a sample-based approximation, namely, Monte Carlo, over the parametric space  $\Xi$ . This leads to

$$\begin{aligned} \mathbb{E}[J^P(\mathcal{W}, \omega)] &\approx \mathbb{E}_{\xi}[J^P(\mathcal{W}, \xi)] = \frac{1}{N} \sum_{i=1}^N J^P(\mathcal{W}, \xi_i) \\ &= \frac{1}{N} \sum_{i=1}^N \int_{\mathcal{D}} f_{\mathcal{W}, M} \cdot u(x, \xi_i) dx + \int_{\Gamma_n} g_M \cdot u(x, \xi_i) ds + \frac{\Lambda}{2} \left( \varsigma - \frac{|\mathcal{W}|}{|\mathcal{D}|} \right)^2, \end{aligned} \quad (28)$$

where  $\{\xi_i\}_{i=1}^N \subset \Xi$  denotes a system of  $N$  samples. Similarly, the stochastic shape derivative expressed in (11) is approximated by

$$\begin{aligned} \mathbb{E}[\mathrm{d}J^P(\mathcal{W}, \omega)(\varphi)] &\approx \mathbb{E}_{\xi}[\mathrm{d}J^P(\mathcal{W}, \xi)(\varphi)] \\ &= \frac{1}{N} \sum_{i=1}^N \left[ \int_{\mathcal{D}} (S_{\omega}^i : \nabla \varphi + T_{\omega}^i \cdot \varphi) dx \right] - \tilde{\Lambda} \int_{\mathcal{W}} \mathrm{div} \varphi dx. \end{aligned} \quad (29)$$

It is well-known that for a standard Monte Carlo estimator as in (28), the error is of the order  $\mathcal{O}(N^{-1/2})$ , which means that a sufficiently large batch size  $N$  is required to accurately estimate the expectation. However, when constructing objective functionals and gradient-like terms, repeatedly solving the linear system obtained from the finite element discretization can be cumbersome with the large batch sizes. Recent advances in machine learning have made stochastic gradient descent (SGD) methods as a proposing alternative approach to alleviating the computational burden of robust shape optimization problems; see, e.g., [24, 36]. The SGD approach produces an unbiased stochastic approximation of the gradient at each optimization step, analogous to the standard Monte Carlo method but using significantly fewer samples. However, in order to control the variance of the underlying quantity of interest, the sample size must still be chosen adequately. Following the strategies proposed in [12, 15], we mitigate this variance by adaptively increasing the

number of samples whenever necessary. In this strategy, we begin with a relatively small sample set of size  $|S| \ll N$ . If the current iteration is likely to yield a meaningful descent direction for the stochastic shape derivative, the sample size is left unchanged. Otherwise, an enlarged sample set is selected based on an a posteriori error indicator that reflects the variance of the sampled stochastic shape derivative  $d\mathcal{J}_i^P$  in (11).

For notation, let  $d\mathcal{J}_i^P$  denote the discrete vector representation of the shape derivative in (29) corresponding to the  $i$ th sample. Then, we define the averaged stochastic shape derivative over a sample set  $S_k$  by

$$d\mathcal{J}_{S_k}^P = \frac{1}{|S_k|} \sum_{i \in S_k} d\mathcal{J}_i^P.$$

Following the methodology of Bollapragada et al. [12], the a posteriori rule for predicting the size of the next sample set  $S_{k+1}$ , referred to as the (practical) *augmented inner product test*, is given by

$$|S_{k+1}| = \lceil \rho |S_k| \rceil, \quad \text{with} \quad \rho = \max(\rho^{IT}, \rho^{OT}). \quad (30)$$

where

$$\begin{aligned} \rho^{IT} &:= \frac{1}{(|S_k| - 1)|S_k| \nu_{IT}^2 \|d\mathcal{J}_{S_k}^P\|^4} \sum_{i \in S_k} ((d\mathcal{J}_i^P)^\top d\mathcal{J}_{S_k}^P - \|d\mathcal{J}_{S_k}^P\|^2)^2, \\ \rho^{OT} &:= \frac{1}{(|S_k| - 1)|S_k| \nu_{OT}^2 \|d\mathcal{J}_{S_k}^P\|^2} \sum_{i \in S_k} \left( \|d\mathcal{J}_i^P\|^2 - \frac{((d\mathcal{J}_i^P)^\top d\mathcal{J}_{S_k}^P)^2}{\|d\mathcal{J}_{S_k}^P\|^2} \right). \end{aligned}$$

Here,  $\nu_{IT}$  and  $\nu_{OT}$  are positive constants and  $\|\cdot\|$  represents the Euclidean-norm. The update rule (30) is applied whenever one of the following conditions fails to hold:

$$\rho^{IT} \leq 1 \quad \text{and} \quad \rho^{OT} \leq 1. \quad (31)$$

Unlike the norm test discussed in [15, 16], the augmented inner product test places prioritizes the creation of descent directions while allowing for more flexibility in its magnitude. Moreover, it ensures that the variance of the sampled gradients in directions orthogonal to the mean gradient is adequately controlled; see [12] for a comprehensive discussion.

### 4.3 Descent direction with level-set method

In the gradient-based optimization process, it is required to find a descent direction  $\theta$  such that  $dJ^P(\mathcal{W}, \xi)(\theta) < 0$  for each  $\xi \in \Xi$ . To find such a descent direction  $\theta \in H^1(\mathcal{D})^2$ , we solve, for every  $\xi \in \Xi$ , the deformation equation [40, 52] given by

$$b(\theta, \varphi) = -dJ^P(\mathcal{W}, \xi)(\varphi) \quad \forall \varphi \in H^1(\mathcal{D})^2, \quad (32)$$

where the positive definite bilinear form  $b : H^1(\mathcal{D})^2 \times H^1(\mathcal{D})^2 \rightarrow \mathbb{R}$  is defined by

$$b(\theta, \varphi) = \int_{\mathcal{D}} (\tau_1 \nabla \theta : \nabla \varphi + \tau_2 \theta \cdot \varphi) dx$$

with constants  $\tau_1, \tau_2 > 0$  and the boundary conditions  $\theta \cdot n = 0$  on  $\partial\mathcal{D}$ . For the weak solution  $H^1(\mathcal{D})^2 \ni \theta \neq 0$  in (32), it follows immediately that

$$dJ^P(\mathcal{W}, \xi)(\theta) = -b(\theta, \theta) < 0 \quad \text{for a.e. } \xi \in \Xi,$$

demonstrating that  $\theta$  is indeed a descent direction.

Once the deformation field  $\theta$  is computed, the shape  $\mathcal{W}$  can be updated by deforming it along this descent direction. However, directly tracking the evolution of the domain boundary under such perturbations can be challenging. To overcome this difficulty, we employ the level-set method introduced in [48], which provides an implicit representation of the geometry. This

implicit formulation greatly simplifies the treatment of topological changes, allowing for the natural creation or merging of holes during the evolution of the shape; see [26]. In the level-set framework, the evolving domain  $\mathcal{W}_t \subset \mathcal{D}$  over a fictitious time interval  $t \in (0, T)$  is characterized by a Lipschitz continuous function  $\psi : \mathcal{D} \times (0, T) \rightarrow \mathbb{R}$ , referred to as the *level-set function*, defined by

$$\begin{cases} \psi(x, t) < 0 & \Leftrightarrow x \in \mathcal{W}, \\ \psi(x, t) = 0 & \Leftrightarrow x \in \partial\mathcal{W} \cap \mathcal{D}, \\ \psi(x, t) > 0 & \Leftrightarrow x \notin \mathcal{D} \setminus \overline{\mathcal{W}}, \end{cases}$$

so that the boundary  $\partial\mathcal{W}_t$  corresponds precisely to the zero level set of  $\psi(x, t)$ .

Let  $x(t) = \Phi_t(x_0)$  denote the trajectory of points on  $\partial\mathcal{W}_t$  originating from an initial configuration  $\mathcal{W}$ , where the motion is governed by the velocity field  $\dot{x}(t) = \theta(x(t))$  with initial position  $x(0) = x_0$ . By differentiating the identity  $\psi(x(t), t) = 0$  with respect to  $t$ , we obtain the following Hamilton–Jacobi type equation (HJE), which describes the evolution of the shape during the optimization procedure

$$\frac{\partial \psi}{\partial t} + \theta \cdot \nabla \psi = 0 \quad \text{in } \mathcal{D} \times (0, T). \quad (33)$$

Consequently, we can state that solving (33) with an appropriate initial level-set function  $\psi(x, 0)$  is equivalent to deforming the boundary of each  $\mathcal{W}_t$  along the descent direction  $-\mathrm{d}J^P(\mathcal{W}_t, \omega)$  for a fixed  $\xi \in \Xi$ .

To keep the computational cost manageable, we solve the Hamilton–Jacobi equation (33) using the Lax–Friedrichs finite difference flux scheme (see [49, 40]) on the rectangular domain  $\mathcal{D} = [0, l_x] \times [0, l_y]$ . For the nodal values  $\psi_{i,j}$  and the deformation vector field  $\theta = (\theta_x, \theta_y)$ , the Lax–Friedrichs flux scheme is given by

$$\widehat{H}^{LF}(p^-, p^+, q^-, q^+) = \frac{\theta_x}{2}(p^+ + p^-) + \frac{\theta_y}{2}(q^+ + q^-) - \frac{|\theta_x|}{2}(p^+ - p^-) + \frac{|\theta_y|}{2}(q^+ - q^-),$$

where the finite difference approximations are

$$\begin{aligned} p^- &= \partial_x^- \psi_{i,j} \approx \frac{\psi_{i,j} - \psi_{i-1,j}}{\Delta x}, & p^+ &= \partial_x^+ \psi_{i,j} \approx \frac{\psi_{i+1,j} - \psi_{i,j}}{\Delta x}, \\ q^- &= \partial_y^- \psi_{i,j} \approx \frac{\psi_{i,j} - \psi_{i,j-1}}{\Delta y}, & q^+ &= \partial_y^+ \psi_{i,j} \approx \frac{\psi_{i,j+1} - \psi_{i,j}}{\Delta y}. \end{aligned}$$

Applying a forward Euler discretization in the fictitious time variable with step size  $\Delta t$ , the fully discrete scheme for the HJE in (33) is equivalent to

$$\psi_{i,j}^{k+1} = \psi_{i,j}^k - \Delta t \widehat{H}^{LF}(p^-, p^+, q^-, q^+). \quad (34)$$

Here, the time step  $\Delta t$  is chosen according to the Courant–Friedrichs–Lowy (CFL) condition and is computed as

$$\Delta t = \alpha_k \frac{\min(\Delta x, \Delta y)}{\theta_{\max}},$$

where  $\alpha_k$  denotes the step length used in the gradient-based optimization algorithm,  $\Delta x = l_x/n_x$  and  $\Delta y = l_y/n_y$  are the spatial grid spacings in the  $x$ - and  $y$ -directions, and  $\theta_{\max} = \|\theta\|_\infty$ . Additionally, the number of fictitious time steps performed at each optimization iteration  $k$  is monitored and adjusted based on the decrease of the objective value  $J^P(\mathcal{W}_k, \xi)$ .

**Remark 2.** To prevent the level-set function  $\psi$  from becoming excessively flat or overly steep during the evolution, one may employ the reinitialization procedure introduced in [18]. This step restores  $\psi$  to a signed-distance-like function while preserving the zero level set. For further implementation details and practical strategies, we refer the reader to [3, 40].

## 4.4 Computation of a practical step length

To update the shapes within the gradient-based optimization framework, we use the iterative scheme

$$\mathcal{W}_{k+1} = (\text{Id} + \alpha_k \theta_k)(\mathcal{W}_k), \quad (35)$$

for  $\mathcal{W}_k \subset \mathcal{D}$  and all  $k \in \mathbb{N}$ . Here,  $\text{Id}$  denotes the identity mapping on  $H^1(\mathcal{D})^2 \cap W^{1,\infty}(\mathbb{R}^2)$ , and  $\alpha_k > 0$  is the step length that scales the deformation field  $\theta_k$  to determine the displacement of points in  $\mathcal{W}_k$ . For determining the step length  $\alpha_k$ , we employ the convergence rule established in [12, Theorem 3.4], which applies to the augmented inner product test presented in Section 4.2.

**Theorem 2.** *Suppose that  $\mathcal{J}(\mathcal{W}) \in C^2(\mathbb{R}^2)$  is bounded below, and that there exists a constant  $L > 0$  such that  $d^2\mathcal{J}(\mathcal{W}) \preceq L$  for all  $\mathcal{W} \in \mathcal{U}^{\text{ad}}$ . Let  $\{\mathcal{W}_k\}$  denote the sequence generated by (35) from an arbitrary initial shape  $\mathcal{W}_0$ , where the mini-batch size  $|S_k|$  is chosen to satisfy the condition (31) exactly for given parameters  $\nu_{IT}, \nu_{OT} > 0$ . If the step length  $\alpha_k$  additionally satisfies*

$$\alpha_k \leq \frac{1}{(1 + \nu_{IT}^2 + \nu_{OT}^2)L}, \quad (36)$$

then

$$\lim_{k \rightarrow \infty} \mathbb{E}[\|d\mathcal{J}(\mathcal{W}_k)\|^2] = 0.$$

Moreover, for any positive integer  $T$ , we have the bound

$$\min_{0 \leq k \leq T-1} \mathbb{E}[\|d\mathcal{J}(\mathcal{W}_k)\|^2] \leq \frac{2}{\alpha T} (\mathcal{J}(\mathcal{W}_0) - \mathcal{J}(\mathcal{W}^*)),$$

where  $\mathcal{W}^*$  denotes the optimal shape within the admissible set  $\mathcal{U}^{\text{ad}}$ .

This theorem implies that the statistical error in the shape derivative can be reduced through an appropriate choice of both the sample size  $|S_k|$  and the step length  $\alpha_k$ . However, selecting an optimal step length requires knowledge of the exact Lipschitz constant  $L$ , which remains unknown in most stochastic optimization settings. To overcome this limitation, we introduce an adaptive strategy that efficiently estimates the Lipschitz constant during the iterative process, motivated by the Lipschitz continuity property of the shape derivative:

$$\mathbb{E}[\|d\mathcal{J}^P(\mathcal{W}_k) - d\mathcal{J}^P(\mathcal{W}_{k-1})\|] \leq L_k d(\mathcal{W}_k, \mathcal{W}_{k-1}), \quad (37)$$

where  $d(\mathcal{W}_k, \mathcal{W}_{k-1})$  quantifies the distance between the current and previous shapes. Then, we approximate the distance measure following the approach in [43] via

$$\widehat{d}(\mathcal{W}_k, \mathcal{W}_{k-1}) = \int_{\mathcal{W}_k} \max_{y \in \mathcal{W}_{k-1}} \|x - y\| dx.$$

Recall that the points are evolved with respect to initial value problem  $\dot{x}(t) = \theta(x(t))$ ,  $x(0) = x_0$ . For each fictitious time duration  $t$ , we have

$$x(t) = x(0) + \int_0^t \theta(x(\tau)) d\tau \approx x(0) + \theta(x(0))t, \quad (38)$$

where  $t > 0$  corresponds to the final time of the discrete HJE problem in (34). Using (38), we get an approximation for the distance between points for each iteration  $k \in \mathbb{N}$  as

$$\begin{aligned} \widehat{d}(\mathcal{W}_k, \mathcal{W}_{k-1}) &= \int_{\mathcal{W}_k} \max_{x_{k-1} \in \mathcal{W}_{k-1}} \|x - x_{k-1}\| dx \\ &\approx \int_{\mathcal{W}_k} \max_{x_{k-1} \in \mathcal{W}_{k-1}} \|\theta(x_{k-1})t\| dx = t \|\theta_{k-1}\|_{\infty} |\mathcal{W}_k|, \end{aligned} \quad (39)$$

where  $\theta_{k-1} := \theta(x_{k-1})$  and  $|\mathcal{W}_k|$  denotes the volume of current shape. Inserting (39) into (37), we find an estimate for  $L_k$

$$L_k = \frac{\mathbb{E}[\|d\mathcal{J}^P(\mathcal{W}_k) - d\mathcal{J}^P(\mathcal{W}_{k-1})\|]}{d(\mathcal{W}_k, \mathcal{W}_{k-1})} \approx \frac{\sum_{i \in S_k} \|d\mathcal{J}_i^P(\mathcal{W}_k) - d\mathcal{J}_i^P(\mathcal{W}_{k-1})\|}{t \|\theta_{k-1}\|_{\infty} |\mathcal{W}_k| |S_k|}. \quad (40)$$

Finally, we obtain an adaptive selection for the step length  $\alpha_k$  by substituting (40) into (36).

## 4.5 Approximation in the spatial domain

Let  $\{\mathcal{T}_h\}_h$  be a quasi-uniform family of triangulations of  $\mathcal{D}$  such that  $\bar{\mathcal{D}} = \bigcup_{K \in \mathcal{T}_h} \bar{K}$ . We define the mesh parameter by  $h = \max_{K \in \mathcal{T}_h} h_K$ , where  $h_K$  denotes the diameter of the element  $K$ . Moreover, let  $\mathcal{E}_h$  denote the partition of the boundary  $\partial\mathcal{D}$  induced by  $\mathcal{T}_h$ , meaning that each  $E \in \mathcal{E}_h$  with  $E \subset \partial\mathcal{D}$  is an edge of some element  $K \in \mathcal{T}_h$ . Denoting the set of all linear polynomials on  $K$  by  $\mathbb{P}(K)$ , we introduce the finite element space

$$V_h = \{v \in C(\mathcal{D})^2 : v_h|_K \in \mathbb{P}(K) \quad \forall K \in \mathcal{T}_h, \text{ and } v_h|_{\Gamma_d} = 0\} \subset H_d^1(\mathcal{D})^2.$$

After applying the KL expansion to the random fields and employing the Monte Carlo approximation, the discrete weak formulation of the system (3) for a fixed sample is as follows: Find  $u_h \in V_h$  such that

$$a(u_h, v) = l(v) \quad \forall v \in V_h, \quad (41)$$

where

$$a(u, v) = \int_{\mathcal{D}} A_{\mathcal{W}, M} \nabla^s u : \nabla^s v \, dx, \quad l(v) = \int_{\mathcal{D}} f_{\mathcal{W}, M} \cdot v \, dx + \int_{\Gamma_n} g_M \cdot v \, ds,$$

see, e.g., [13, Chapter 11] for existence and uniqueness of the Galerkin solutions.

To generate a sequence of meshes  $\{\mathcal{T}_h^k\}_{k \geq 0}$  in an adaptive manner, we use the dual-weighted residual (DWR) framework [8, 10]. In this goal-oriented mesh adaptation strategy, one aims to control the error in a quantity of interest (QoI)  $\mathcal{Q} : V \rightarrow \mathbb{R}$  for some Hilbert space  $V$ :

$$|\mathcal{Q}(u) - \mathcal{Q}(u_h)| = \eta \leq \text{tol},$$

for a prescribed tolerance  $\text{tol} > 0$ . For completeness, we now recall the corresponding error representation formula, whose proof can be found in [10, 8].

**Proposition 2.** *For a goal functional  $\mathcal{Q}$ , the following a posteriori expression is valid*

$$\mathcal{Q}(u) - \mathcal{Q}(u_h) = \frac{1}{2} r(z - I_h z) + \frac{1}{2} r^*(u - I_h u) + E \quad \forall I_h z, I_h u \in V_h$$

where  $r$  and  $r^*$  are residuals of the primal and dual problems, respectively, and the remainder term is given by  $E = \frac{1}{2} \int_0^1 (\delta_u^3 \mathcal{Q}(\lambda u - (1 - \lambda)u_h), e, e, e) \lambda(1 - \lambda) \, d\lambda$  with the primal error  $e = u - u_h$ . Moreover, if  $\mathcal{Q}$  is a linear functional, then the primal and dual residuals coincide, i.e.,  $r = r^*$ , and the error representation simplifies to

$$\mathcal{Q}(u) - \mathcal{Q}(u_h) = r(z - I_h z) \quad \forall I_h z \in V_h. \quad (42)$$

To obtain optimal designs that are comparable to those computed on highly refined fixed meshes, we also account for the discretization errors arising from the deformation bilinear form (32), providing the descent directions, in addition to the discretization errors associated with the constraint PDE, namely the linear elasticity system (3). Consequently, it becomes necessary to introduce multiple goal functionals that correspond to these distinct sources of error.

Our first goal functional is the compliance, defined by  $\mathcal{Q}^c = J(\mathcal{W}, \xi)$  for any sample  $\xi \in \Xi$ . For  $v \in H_d^1(\mathcal{D})^2$ , the primal and dual residuals are given by

$$r(v) = l(v) - a(u_h, v) \quad \text{and} \quad r^*(v) = (\delta_u \mathcal{Q}^c(u_h), v) - a^*(z_h, v),$$

respectively, for the primal solution  $u_h$  and the dual solution  $z_h$ , which solves

$$a^*(z_h, v) = (\delta_u \mathcal{Q}^c(u_h), v) \quad \forall v \in V_h, \quad (43)$$

where  $\delta_u$  denotes the directional derivative in the direction of  $u$ . In view of the discrete weak form (41) and (43), the primal and dual residuals satisfy the Galerkin orthogonality relations

$$r(v_h) = r^*(v_h) = 0 \quad \forall v_h \in V_h.$$

By applying integration by parts to the elementwise contributions  $K \in \{\mathcal{T}_h\}_h$  of the residuals  $r$  and  $r^*$ , and using the Cauchy–Schwarz inequality, we arrive at the estimate

$$|\mathcal{Q}^c(u) - \mathcal{Q}^c(u_h)| \leq \sum_{K \in \mathcal{T}_h} \underbrace{\rho_K^u \omega_K^z}_{\eta_K^u} + \underbrace{\rho_K^z \omega_K^u}_{\eta_K^z} := \eta^c,$$

where the element residuals  $\rho_K^z, \rho_K^u$  are

$$\begin{aligned} \rho_K^u &= \|f_{\mathcal{W},M} + \operatorname{div}(A_{\mathcal{W},M} \nabla^s u_h)\|_K + h_K^{-1/2} \|\llbracket (A_{\mathcal{W},M} \nabla^s u_h) n \rrbracket\|_{\partial K}, \\ \rho_K^z &= \|\delta_u \mathcal{Q}^c(u_h) + \operatorname{div}(A_{\mathcal{W},M} \nabla^s z_h)\|_K + h_K^{-1/2} \|\llbracket (A_{\mathcal{W},M} \nabla^s z_h) n \rrbracket\|_{\partial K}, \end{aligned}$$

and the corresponding local weights  $\omega_K^u$  and  $\omega_K^z$  are given by

$$\omega_K^u = \|u - I_h u\|_K + h_K^{1/2} \|u - I_h u\|_{\partial K}, \quad \omega_K^z = \|z - I_h z\|_K + h_K^{1/2} \|z - I_h z\|_{\partial K},$$

where the local mesh size is defined by  $h_K = |K|^{1/2}$  and  $\llbracket \cdot \rrbracket$  denotes jump across interelement sides, defined by

$$\llbracket (A_{\mathcal{W},M} \nabla^s u_h) n \rrbracket|_E = \frac{1}{2} ((A_{\mathcal{W},M} \nabla^s u_h) n|_{K_1} - (A_{\mathcal{W},M} \nabla^s u_h) n|_{K_2})$$

for  $E \in K_1 \cap K_2$  with  $K_1, K_2 \in \mathcal{T}_h$ , and  $n$  is unit normal vector to  $\partial K_1$ . On the Neumann boundary  $\Gamma_n$ , the jump is set to  $\llbracket (A_{\mathcal{W},M} \nabla^s u_h) n \rrbracket = g_M - (A_{\mathcal{W},M} \nabla^s u_h) n$ .

**Remark 3.** We note that the underlying quantity of interest  $\mathcal{Q}^c = J(\mathcal{W}, \xi)$  is a linear functional. Therefore, the error representation simplifies, and in our numerical simulations we employ the bound

$$|\mathcal{Q}^c(u) - \mathcal{Q}^c(u_h)| \leq \sum_{K \in \mathcal{T}_h} \eta_K^c = \sum_{K \in \mathcal{T}_h} \rho_K^u \omega_K^z, \quad (44)$$

see, cf. Proposition 2.

Motivated by the role of the shape derivative  $dJ^P(\mathcal{W})$  in updating the geometry of the current mesh  $\mathcal{W}$ , we introduce a second goal functional to control the deformation error. Specifically, we define

$$\mathcal{Q}^d(\theta) = -dJ^P(\mathcal{W})(\theta),$$

which quantifies the accuracy of the deformation field used to evolve the shape. By using (42) with the symmetricity of  $b(\theta, \varphi)$  in (32) and the linearity of  $\mathcal{Q}^d(\theta)$ , we get

$$\begin{aligned} \mathcal{Q}^d(\theta) - \mathcal{Q}^d(\theta_h) &= -dJ^P(\mathcal{W})(\zeta - I_h \zeta) - b(\theta_h, \zeta - I_h \zeta) \\ &=: r^d(\zeta - I_h \zeta), \quad \forall \zeta \in H^1(\mathcal{D})^2, \forall I_h \zeta \in V_h, \end{aligned} \quad (45)$$

where

$$\begin{aligned} r^d(\zeta - I_h \zeta) &= - \int_{\mathcal{D}} (S_{\omega} : \nabla(\zeta - I_h \zeta) + T_{\omega} \cdot (\zeta - I_h \zeta)) dx \\ &\quad - \tilde{\Lambda} \int_{\mathcal{W}} \operatorname{div}(\zeta - I_h \zeta) dx \\ &\quad - \int_{\mathcal{D}} (\tau_1 \nabla \theta_h : \nabla(\zeta - I_h \zeta) + \tau_2 \theta_h \cdot (\zeta - I_h \zeta)) dx, \end{aligned}$$

with  $\tilde{\Lambda} = \frac{\Lambda}{|\mathcal{D}|} \left( \eta - \frac{|\mathcal{W}|}{|\mathcal{D}|} \right)$ . Here, both  $S_{\omega}$  and  $T_{\omega}$  depend on  $u_h$ , that is,  $S_{\omega} := S_{\omega}(u_h)$  and  $T_{\omega} := T_{\omega}(u_h)$ , as the discrete primal solution  $u_h$  is utilized to address the auxiliary variational

problem (32). Moreover,  $\zeta$  denotes dual solution of the auxiliary variational form (32). By applying the integration by part over  $K \in \mathcal{T}_h$ , we obtain

$$\begin{aligned} r^d(\zeta - I_h \zeta) &= \sum_{K \in \mathcal{T}_h} \int_{\partial K} \llbracket -\tau_1 \nabla \theta_h \cdot n \rrbracket \cdot (\zeta - I_h \zeta) \, ds \\ &\quad + \sum_{K \in \mathcal{T}_h} \int_K \left( (\tilde{\Lambda} \chi_{\mathcal{W}} \mathbf{Id} - S_{\omega}) : \nabla (\zeta - I_h \zeta) \right. \\ &\quad \left. + (\tau_1 \operatorname{div}(\nabla \theta_h) - \tau_2 \theta_h - T_{\omega}) \cdot (\zeta - I_h \zeta) \right) \, dx. \end{aligned}$$

Then, an application of divergence theorem for the tensor  $\tilde{\Lambda} \chi_{\mathcal{W}} \mathbf{Id} - S_{\omega}$  on each  $K \in \mathcal{T}_h$  yields

$$\begin{aligned} r^d(\zeta - I_h \zeta) &= \sum_{K \in \mathcal{T}_h} \int_{\partial K} \llbracket -(\tau_1 \nabla \theta_h + S_{\omega} - \tilde{\Lambda} \chi_{\mathcal{W}} \mathbf{Id}) n \rrbracket \cdot (\zeta - I_h \zeta) \, ds \\ &\quad + \sum_{K \in \mathcal{T}_h} \int_K \left( (\operatorname{div}(\tau_1 \nabla \theta_h + S_{\omega}) - \tau_2 \theta_h - T_{\omega}) \cdot (\zeta - I_h \zeta) \right) \, dx. \end{aligned} \quad (46)$$

Inserting (46) into (45), we obtain a dual-weighted residual error indicator

$$|\mathcal{Q}^d(\theta) - \mathcal{Q}^d(\theta_h)| \leq \sum_{K \in \mathcal{T}_h} \rho_K^\theta \omega_K^\zeta := \eta^d, \quad (47)$$

where the element residual  $\rho_K^\theta$  and the local weight  $\omega_K^\zeta$  are given, respectively, by

$$\begin{aligned} \rho_K^\theta &= \|\operatorname{div}(\tau_1 \nabla \theta_h + S_{\omega}) - \tau_2 \theta_h - T_{\omega}\|_K \\ &\quad + h_K^{-1/2} \|\llbracket -(\tau_1 \nabla \theta_h + S_{\omega} - \tilde{\Lambda} \chi_{\mathcal{W}} \mathbf{Id}) n \rrbracket\|_{\partial K}, \\ \omega_K^\zeta &= \|\zeta - I_h \zeta\|_K + h_K^{1/2} \|\zeta - I_h \zeta\|_{\partial K}. \end{aligned}$$

To obtain fully a posteriori error estimators in (44) and (47), it is necessary to approximate the exact dual solutions. To address this, we employ an extrapolation strategy for the Galerkin approximations  $z_h, \zeta_h \in V_h$ . Let  $\tilde{V}_h \supset V_h$  denote an enriched (higher-order) finite element space defined on the same triangulation  $\mathcal{T}_h$ . We then introduce an extrapolation operator  $E : V_h \rightarrow \tilde{V}_h$  that maps the discrete dual solutions to higher-order approximations  $Ez_h, E\zeta_h \in \tilde{V}_h$ , thereby enhancing their accuracy. Finally, following [28], we balance the contributions of the different goal functionals by scaling them, and define the combined quantity

$$\mathcal{Q} = \frac{|\mathcal{Q}^c(u) - \mathcal{Q}^c(u_h)|}{|\mathcal{Q}^c(u_h)|} + \frac{|\mathcal{Q}^d(\theta) - \mathcal{Q}^d(\theta_h)|}{|\mathcal{Q}^d(\theta_h)|}.$$

## 5 Adaptive procedure

In this section, we present a fully adaptive procedure for solving the robust shape optimization problem (5) in Algorithm 1 and also provide detailed descriptions of the algorithm's subroutines. Recall that  $k \geq 1$  stands for the optimization iteration, and  $\mathcal{W}_k$  is the current shape with deformable boundary  $\partial \mathcal{W}_k$ . The associated finite element space for this shape is given by  $V_h^k = V_h(\mathcal{T}_h^k)$ .

At the beginning of the procedure, the KL expansion (27) is generated in the subroutine `compute_kle` using the (exact) eigenpairs  $\{(\lambda_i, b_i)\}_{i=1}^M$ . In the subroutine `solve_weak_forms`, we then solve the primal problems (4) and (32), along with their corresponding dual problems, by employing the finite element space  $V_h^k$  associated with the current shape  $\mathcal{W}_k$ . Next, the dual-weighted residual estimators given in (44) and (47) are computed in the subroutine `estimate_dwr`.

---

**Algorithm 1** An adaptive framework for robust shape optimization.

---

**Require:** Initialize the working domain  $\mathcal{D}$ , the level-set function  $\psi^0$ , the parameters  $\alpha_0, \nu_{OT}, \nu_{IT}, \Lambda, \varsigma, \epsilon, \tau_1, \tau_2 > 0$ , the initial batch-size  $|S_0|$ , the eigenpair  $\{(\lambda_i, b_i)\}_{i=1}^M$ , the initial triangulation  $\mathcal{T}_h^0$  with the initial mesh size  $h^0$ , the reference mesh size  $h^*$ , tolerance  $\text{tol}_\eta$ .

1:  $\mathcal{W}_0 \leftarrow \{x \in \mathcal{D} : \psi^0(x) < 0\}$   
2:  $\theta_0 \leftarrow 0, k \leftarrow 0$   
3:  $\xi \leftarrow \text{compute\_kle}(\lambda_i, b_i)$   
4: **while** stopping conditions are not met **do**  
5:   **for**  $i = 0, \dots, |S_k| - 1$  **do**  
6:      $u_h^i, z_h^i, \theta_h^i, \zeta_h^i \leftarrow \text{solve\_weak\_forms}(\mathcal{T}_h^k, \mathcal{W}_k, \xi^i)$   
7:      $\eta_K^{c,i}, \eta_K^{d,i} \leftarrow \text{estimate\_dwr}(\mathcal{T}_h^k, \mathcal{W}_k, u_h^i, z_h^i, \theta_h^i, \zeta_h^i, \xi^i)$   
8:      $(J_k^P)^i \leftarrow \text{compute\_cost}(\mathcal{T}_h^k, \mathcal{W}_k, u_h^i, \xi^i)$   
9:      $(dJ_k^P)^i \leftarrow \text{compute\_shape\_deivative}(\mathcal{T}_h^k, \mathcal{W}_k, u_h^i, z_h^i, \theta_h^i, \xi^i)$   
10:   **end for**  
11:   Apply a sample approximation with sample size  $S_k$  to get  $\eta_k^{S_k}, (J_k^P)^{S_k}, (dJ_k^P)^{S_k}$ , and  $\theta_h^{S_k}$ .  
12:   **if**  $\eta_k^{S_k}(\eta_K^c, \eta_K^d) > \text{tol}_\eta$  **and**  $h_{\min}(\mathcal{T}_h^k) > h^*$  **then**  
13:      $\mathcal{T}_h^{k+1} \leftarrow \text{mark\_and\_refine}(\mathcal{T}_h^k, \eta_k^{S_k})$ , and **go to** Step 4  
14:   **end if**  
15:    $|S_k| \leftarrow \text{estimate\_sample\_size}((dJ_k^P)^{S_k}, (dJ_k^P)^i, \nu_{IT}, \nu_{OT})$   
16:   **if**  $k > 1$  **then**  
17:      $\alpha_k \leftarrow \text{estimate\_step\_length}((dJ_k^P)^{S_k}, dJ_k^{S_k-1}, \mathcal{W}_k)$   
18:   **end if**  
19:    $\mathcal{T}_h^{k+1} \leftarrow \text{reset\_mesh}(\mathcal{T}_h^k)$   
20:    $\psi^{k+1} \leftarrow \text{solve\_hje}(\psi^k, \theta_h^{S_k}, \alpha_k)$   
21:    $\mathcal{W}_{k+1} \leftarrow \{x \in \mathcal{D} : \psi^{k+1}(x) < 0\}$   
22:    $\theta_{k+1} \leftarrow \theta_k$  and  $k \leftarrow k + 1$   
23: **end while**

---

During the computation of the corresponding error indicators, it is additionally necessary to solve the dual problems

$$a^*(z_h, v) = (\delta_u \mathcal{Q}^c(u_h), v) \quad \text{and} \quad b^*(\zeta_h, \varphi) = (\delta_\theta \mathcal{Q}^d(\theta_h), \varphi) \quad \forall v, \varphi \in \tilde{V}_h^k,$$

where  $\tilde{V}_h^k$  denotes the enriched finite element space obtained by using quadratic polynomial order. Then, the penalized compliance cost (28) and the corresponding shape derivative (29) for the given realization  $\xi$  are evaluated at the subroutines `compute_cost` and `compute_shape_derivative`, respectively. The subroutine `mark_and_refine` selects elements of  $\mathcal{T}_h^k$  to be refined using the bulk marking strategy of Dörfler [27], and then refines the marked elements by bisection while preserving the conformity of  $\mathcal{T}_h^k$ . This refinement is performed if the scaled error indicator  $\eta_k^{S_k}$  exceeds the tolerance value  $\text{tol}_\eta$ , or if the current mesh size has not yet reached the prescribed minimum size  $h^*$ .

After updating the current mesh  $\mathcal{T}_h^k$ , we apply the augmented inner product criterion described in Section 4.2 to determine whether the sample size  $|S_k|$  should be increased in the subroutine `estimate_sample_size`. Before updating the current shape  $\mathcal{W}_k$ , the step length  $\alpha_k$  is computed using (36), which depends on the estimated Lipschitz constant  $L_k$  given in (40). Then, the mesh is reset to the original initial triangulation to simplify the shape update process. Once the Hamilton–Jacobi equation (33) is solved using a finite difference scheme in the subroutine `solve_hje`, the boundary of the shape  $\mathcal{W}_k$  is updated accordingly. This iterative procedure is repeated until one of the stopping criteria is satisfied:  $\max_{1 \leq i \leq 5} \{|\mathcal{J}_k^P - \mathcal{J}_{k-i}^P| \leq 0.01 \mathcal{J}_k^P\}$ ,  $|\mathcal{W} - \mathcal{V}^*| \leq 0.005$ , or the maximum number of iterations is reached.

**Remark 4.** *Mesh coarsening plays a role as important as mesh refinement in level-set-based methods, as it allows the computational mesh to adapt to the evolving level-set interface by removing unnecessary fine elements, thereby improving efficiency while preserving accuracy. Since mesh coarsening is not currently supported in the FEniCS/DOLFIN framework, we adopt an alternative strategy in Algorithm 1 by resetting the mesh to the initial coarse discretization. While this strategy is adequate for the benchmark problems considered here, a fully integrated coarsening approach will be essential for more complex applications.*

## 6 Numerical experiments

In this section, we present numerical experiments based on typical benchmark problems from aerospace landing systems and legged-robot movement in order to assess the efficiency and robustness of the proposed optimization approach in real-world mechanical scenarios. These application areas are well suited for exemplification because they have random contact interactions, ambiguous loading conditions, and a high level of sensitivity to the geometric features.

One of the main problems in the design of aerospace landing gear is the determination of the structural geometries that can withstand unforeseen impact forces during events like touchdown [38, 60]. In particular, for rotorcraft operating on unprepared terrain and planetary landers, the magnitude and orientation of ground reaction forces may vary significantly due to surface roughness, spatial heterogeneity of material properties, and variations in landing attitude. A typical benchmark scenario consists of a thin landing strut connected to a hard fuselage, with an impulsive load applied at an unknown angle of contact on the bottom half. The load distribution is typically modeled by a stochastic angular range coupled with variations in the peak impact amplitude. Under such uncertain contact scenarios, the resulting optimal designs frequently deviates from simple column-like vertical profiles and, instead, exhibits locally stiffened shapes as truss structures or curvature-induced load spreading features. Owing to these characteristics, this benchmark problem provides an effective test case for demonstrating the capability of the proposed algorithm to account for randomness and uncertainty in structural design.

In legged-robot locomotion, a related set of challenges arises from the periodic contact events that occur during each gait cycle [30]. In contrast to aerospace landing systems, which typically

involve a single touchdown event, legged robots undergo numerous intermittent contacts, each with varying normal and tangential forces. For instance, the contact forces acting on a leg segment of a quadrupedal robot traveling over natural terrain during the stance phase might include shock-like vertical impulses from stepping on uneven ground, lateral stabilizing loads, and forward propulsive components. A typical numerical benchmark in this domain simulates a footpad or a flexible leg segment interacting with a terrain of undetermined height values, where surface slopes and friction coefficients are considered as natural randomness factors. Hence, the resulting shape optimization problem seeks lightweight geometries that enable efficient leg motion while minimizing structural compliance.

In both the aerospace and robotics case studies, landing legs or struts serve as critical structural components whose design directly influences system reliability, load transfer, and energy absorption under impact conditions. Numerical experiments typically evaluate performance measures such as maximum von Mises stress, tip deflection under multi-directional loading, or compliance functionals associated with stochastic contact force ensembles. Accordingly, the present test cases focus on the shape optimization of leg-like structures and struts to minimize compliance during touchdown in the presence of random contact forces. We analyze the behavior of the algorithm in three scenarios: a randomness study on a fixed mesh, a mesh refinement study using full Monte Carlo sampling, and a fully adaptive framework that integrates both adaptive sampling and adaptive meshing strategies.

In the finite element approximation of the solutions, linear Lagrange elements are constructed on the crossed triangulation  $\mathcal{T}_h$ , resulting in  $2(n_x + 1)(n_y + 1) + 2n_x n_y$  degrees of freedom (DoF). For the discretization of the probabilistic domain, random fields are represented by a truncated Gaussian Karhunen–Loëve (KL) expansion with a separable exponential covariance function

$$\mathcal{C}_\kappa(x, \tilde{x}) = \kappa_\kappa^2 \prod_{j=1}^2 e^{-|x_j - \tilde{x}_j|/\ell_j},$$

where  $\ell_j$ ,  $j = 1, 2$ , and  $\kappa_\kappa$  represent the correlation length and the standard deviation, respectively, on the physical working domain  $\mathcal{D} = [0, l_x] \times [0, l_y]$ . Unless otherwise stated, the parameters used in the simulations are provided in Table 1. All computations are carried out on an Intel(R) Core(TM) i5-6500 @ 3.20 GHz processor with 8 GB RAM, using the FEniCS/DOLFIN library and based on the implementation developed by Laurain [40].

Table 1: Descriptions of the parameters used in the simulations.

Parameter	Description	Value
$\epsilon$	weak material constant in (2)	$10^{-3}$
$\varsigma$	fraction parameter in (6)	0.3
$\Lambda$	penalization constant in (10)	500
$\nu_{IT}$	inner product test constant in (30)	0.6
$\nu_{OT}$	orthogonality test constant in (30)	$5.8 \approx \tan 80^\circ$
$\tau_1, \tau_2$	positive constants in (32)	$10^3, 1$
$S_0$	initial sample size	2
$\alpha_0$	initial step length	0.01
$\ell$	correlation length	1
$\text{tol}_\eta$	tolerance for the estimator	0.1
$h^*$	reference mesh size	1/180

As a benchmark example, we consider the compliance minimization of carrier legs in aerospace or robotic structures. In this setting, the isotropic materials with dummy material parameters are given by

$$\mu = \frac{E}{2(1 + \nu)} \quad \text{and} \quad \lambda = \frac{E\nu}{(1 + \nu)(1 - 2\nu)},$$

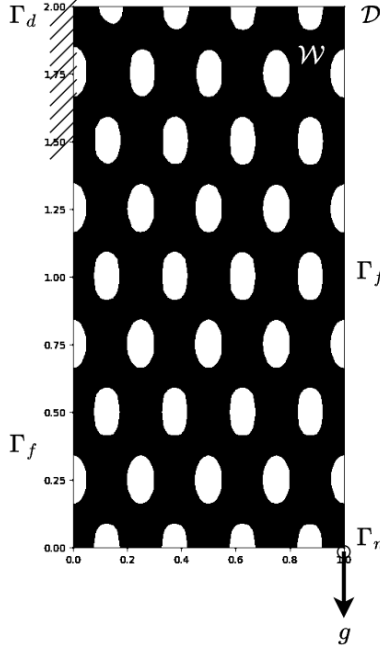


Figure 1: Initial level-set function defined on the computational domain  $\mathcal{D}$ , including the prescribed boundary conditions and an applied load force  $g$  at  $(0, 1)$ .

where the Young's modulus is set to  $E = 1$  and the Poisson's ratio to  $\nu = 0.3$ . We assume that there is no body force, that is,  $f = 0$ . The initial mesh is generated using  $n_x = 60$  and  $n_y = 120$ , resulting in  $2 \times 14,581$  degrees of freedom (DoF). With correlation lengths chosen as  $\ell_1 = \ell_2 = 1$ , we compute the first  $M$  eigenpairs  $\{(\lambda_i, b_i)\}_{i=1}^M$  of the KL expansion to capture 90% of the total energy, with an upper bound of  $M_{\max} = 100$ . Further, the random loading (i.e., contact force) is prescribed as

$$g = (10 \cos \phi, 10 \sin \phi),$$

where the random loading angle is realized through

$$\phi = \bar{\phi} + \kappa_\phi \sum_{i=1}^M \sqrt{\lambda_i} b_i(x) \xi_i,$$

with mean angle  $\bar{\phi} = 90^\circ$  and standard deviation  $\kappa_\phi \in \{5^\circ, 10^\circ, 30^\circ\}$ . Here,  $\xi = (\xi_1, \dots, \xi_M)$  denotes an i.i.d. vector of Gaussian random variables satisfying  $\xi_i \sim \mathcal{N}(0, 1)$ . The load  $g(x, \omega)$  is applied at the point  $(1, 0)$ , i.e., on the boundary segment  $\Gamma_n = \{1\} \times \{0\}$ . The Dirichlet boundary is specified as  $\Gamma_d = \{0\} \times [1.5, 2]$ , while the remaining part of the boundary is taken as the free boundary  $\Gamma_f$ . Further, the initial domain  $\mathcal{W}_0$  is constructed by employing the initial level-set function is given by  $\psi^0(x, y) = -\cos(8\pi x) \cos(4\pi y) - 0.5$  as illustrated in Figure 1.

To compare the results obtained from the numerical experiments, we introduce a computational index defined as

$$\text{CI} \propto \sum_{i=1}^M \sum_{j=1}^Q N_i \varrho(d_{ij}), \quad (48)$$

where  $d_{ij}$  denotes the number of degrees of freedom at the  $i$ th optimization step and the  $j$ th mesh refinement level, while  $N_i$  is the number of Monte Carlo samples used at the  $i$ th optimization step. The function  $\varrho$  represents the time complexity of the linear solver in terms of the overall problem size. As the main linear solver, we use the MUMPS implementation available in FEniCS/DOLFIN, which has a computational complexity of  $O(d^{3/2})$ ; see, e.g., [4].

## 6.1 Randomness study

We first investigate the effect of loading under various loading-angle deviations. This range of angles reflects scenarios in which the landing approach is maintained despite substantial deviations or when leg strokes occur on terrain with differing levels of roughness. Accordingly, we present the optimized shapes obtained for  $\kappa_\phi \in \{5^\circ, 10^\circ, 30^\circ\}$  in Figure 2.

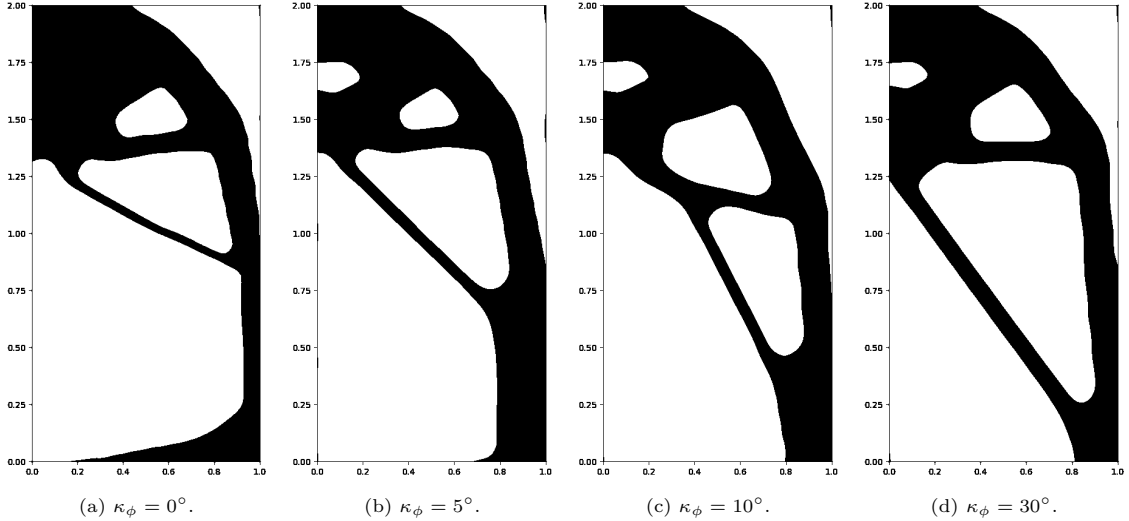


Figure 2: Final optimized designs obtained for various loading-angle deviations  $\kappa_\phi$  using full Monte Carlo sampling on a fixed mesh.

Next, we explore the effect of randomness on a fixed mesh and demonstrate the superiority of the adaptive sampling strategy discussed in Section 4.2. Figure 3 shows the final designs obtained with the loading-angle deviation  $\kappa_\phi = 30^\circ$  using adaptive and full sampling. It is observed that the final designs produced by full sampling and adaptive sampling are almost identical. However, the computational effort is reduced significantly when adaptive sampling is employed; see Table 2. According to the CI estimates in Table 2, gradually increasing the sample size, rather than using the full sample set at every iteration, reduces the computational cost significantly, while still producing reasonable approximations of the mean and standard deviation obtained from full Monte Carlo sampling; see, Figure 4.

Table 2: Comparison of the computational effort for full and adaptive sampling approaches in terms of the number of samples, computational runtime, and the computational index defined in (48).

	DoF	$N$	$T_{\text{total}}[\text{hours}]$	CI
full sampling	29,162	10	6.32	$14.9 \cdot 10^9$
adaptive sampling	29,162	$2 \rightarrow 7$	3.27	$8.76 \cdot 10^9$

## 6.2 Mesh refinement study

Next, we investigate the effect of mesh refinement under the full sampling setting. Three types of meshes are considered: the fixed coarse mesh with 29,162 DoF, the fixed fine mesh with 260,282 DoF, and the adaptively generated mesh refined from 29,162  $\rightarrow$  43,392 DoF. Table 3 presents a comparison of the computational effort associated with these mesh configurations. The results show that the adaptive refinement strategy substantially reduces computational cost while successfully capturing the discretization behavior of both the compliance problem indicators and

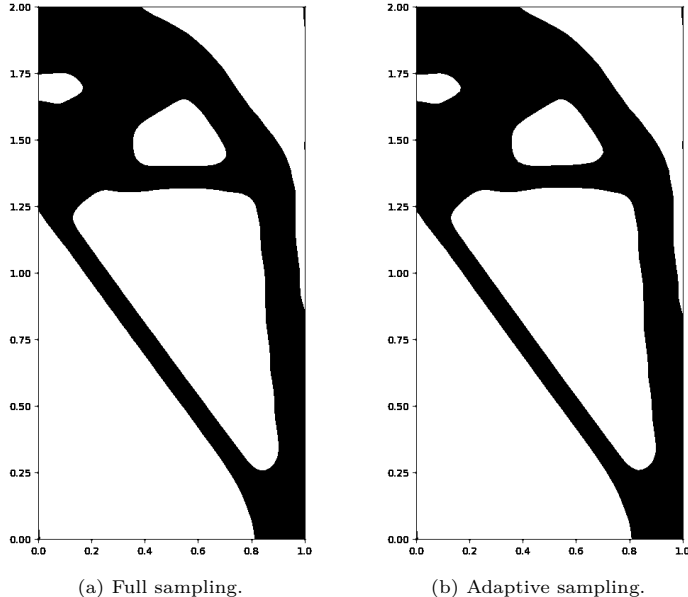


Figure 3: Final optimized designs on a fixed mesh using full and adaptive sampling approaches for a loading-angle deviation of  $\kappa_\phi = 30^\circ$ .

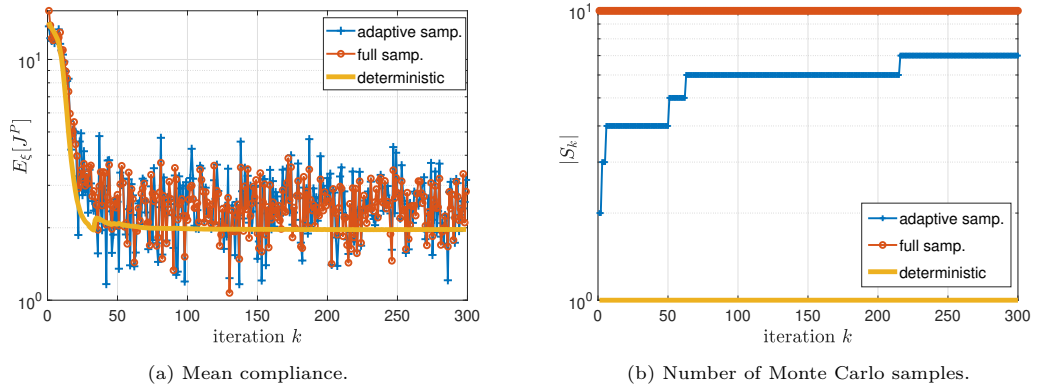


Figure 4: Evolution of the mean compliance  $\mathbb{E}_\xi[J^P]$  and the size of Monte Carlo set  $|S_k|$  for deterministic and random loading angles ( $\kappa_\phi = 30^\circ$ ) on a fixed mesh.

the shape derivative indicators, achieving accuracy comparable to the fixed fine mesh. See Figure 5 and Table 4 for the behavior of the compliance functional and the final values of the shape optimization variables. Furthermore, the resulting final designs are displayed in Figure 6.

Table 3: Comparison of the computational effort between the fixed coarse mesh, fixed fine mesh, and adaptively generated mesh under full sampling in terms of the degrees of freedom, computational runtime, and the computational index defined in (48).

	DoF	$N$	$T_{\text{total}}[\text{hours}]$	CI
fixed coarse mesh	29,162	10	6.32	$14.9 \cdot 10^9$
fixed fine mesh	260,282	10	51.0	$397 \cdot 10^9$
adaptive mesh	$29,162 \rightarrow 43,392$	10	17.2	$41.9 \cdot 10^9$

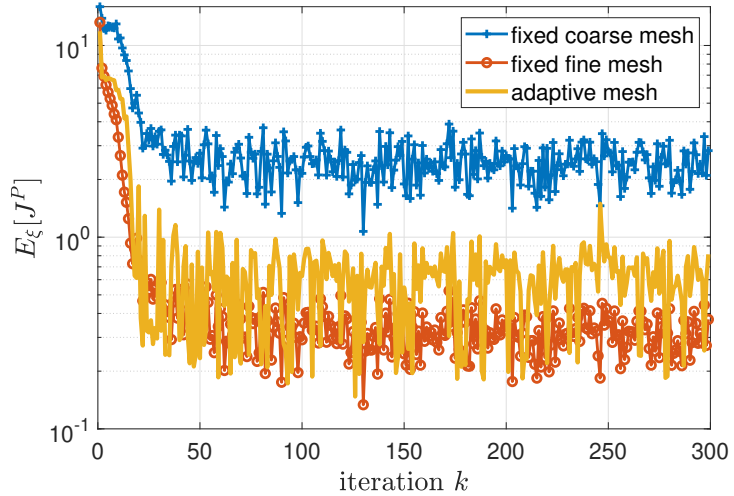


Figure 5: Evolution of mean compliance  $\mathbb{E}_\xi[J^P]$  obtained using the fixed coarse mesh, the fixed fine mesh, the adaptively generated mesh with full sampling.

Table 4: Comparison of the final shape optimization variable values across the meshes used in the refinement study.

Variable	Adaptive	Coarse Mesh	Fine Mesh
$\mathbb{E}_\xi[J^P]$	0.81	2.83	0.37
$\eta^c + \eta^d$	0.009	0.112	0.002
$\eta^c$	0.05	0.18	0.02
$\eta^d$	0.11	0.39	0.04
$\alpha_k$	0.008	0.016	0.016
$\mathbb{E}_\xi[dJ^P]$	9.83	20.22	6.99
$\mathbb{V}_\xi[dJ^P]$	123.7	482.8	64.7

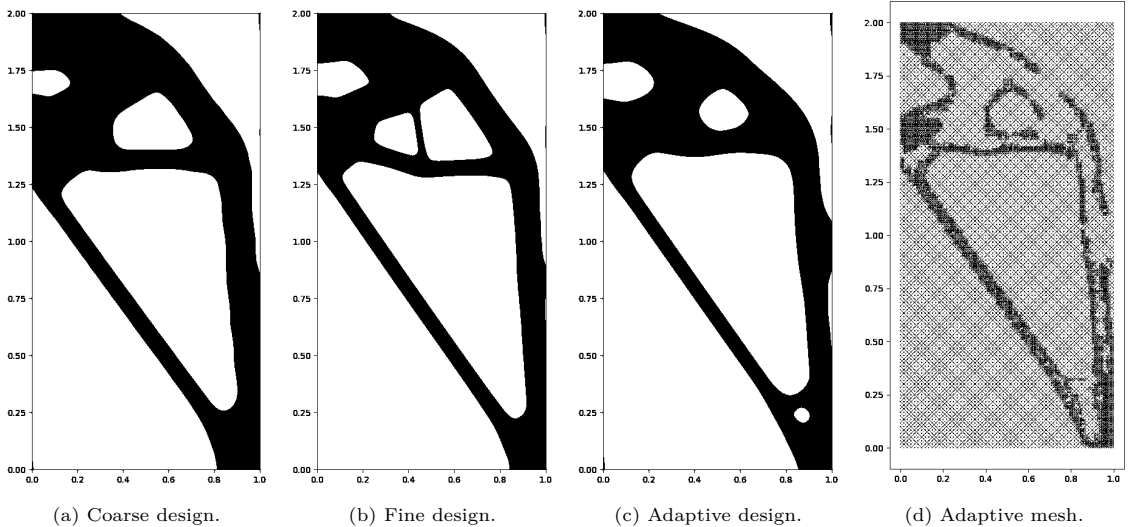


Figure 6: Final optimized designs obtained on a fixed coarse mesh with 29,162 degrees of freedom (a), on a fixed fine mesh with 260,282 degrees of freedom (b), and on an adaptively generated mesh with 43,392 degrees of freedom (c). The corresponding adaptive mesh is shown in (d).

### 6.3 Full adaptivity study

Last, we employ both adaptive sampling and adaptive mesh refinement. Compared with the fixed mesh under full Monte Carlo sampling, the fully adaptive setting is able to accurately capture the statistics of the random solution while using substantially fewer samples and degrees of freedom (DoF); see Figure 7 and Table 5. Moreover, the adaptive procedure simultaneously balances the discretization errors and the computational complexity associated with the physical domain discretization, as expected. In the numerical simulations, the total elapsed time for the fixed fine mesh with 260,282 DoF under full sampling is 51.0 hours, whereas the fully adaptive case, refined from 29,162  $\rightarrow$  43,378 DoF, requires only 8.72 hours; see Table 6. In terms of the CI comparison, the fully adaptive optimization reduces the computational effort needed to reach the fully refined optimum shape by nearly one order of magnitude. Finally, the resulting final designs are displayed in Figure 8.

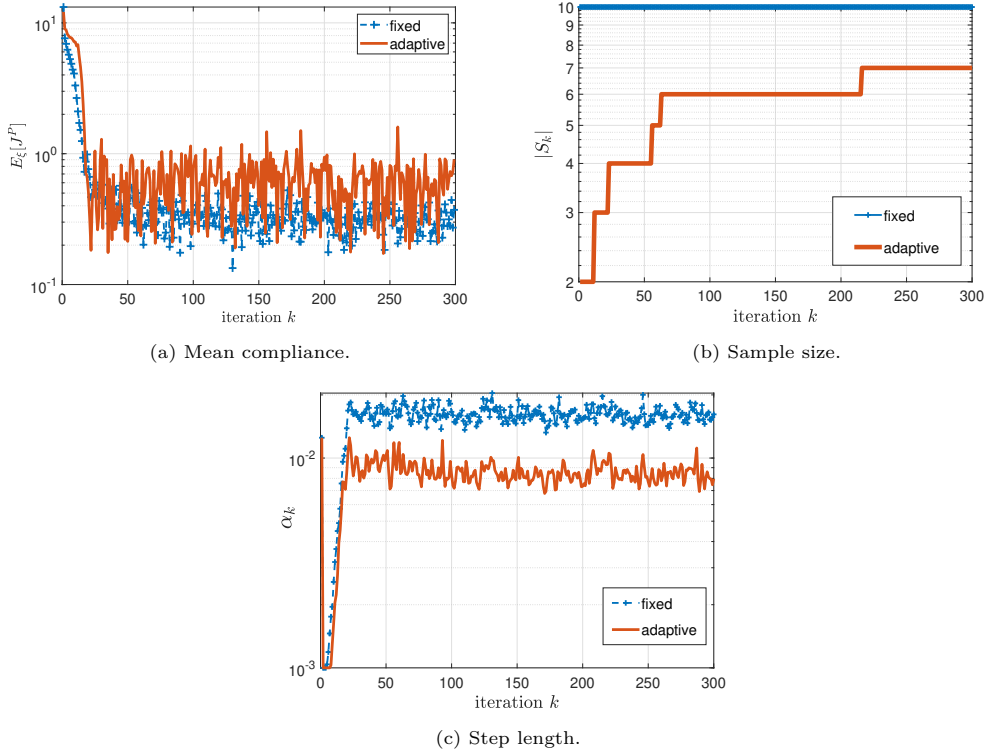


Figure 7: Evolution of the mean compliance  $\mathbb{E}_\xi[J^P]$ , the Monte Carlo sample size  $|S_k|$ , and the step length  $\alpha_k$  for the fixed and adaptive approaches.

## 7 Conclusion

In this paper, we have presented an adaptive framework to address the robust shape optimization governed by a linear elasticity model that incorporates uncertainties in both loading and material parameters. The existence and derivation of the shape derivative associated with the expected compliance minimization problem, subject to a penalized volume constraint is shown. Within this adaptive framework, the number of Monte Carlo samples, the mesh resolution, and the step length in the gradient-based optimization are all controlled by a posteriori error estimators. In addition, we have employed a multi-goal-oriented estimator derived from the discretization of the constraint PDE and the deformation bilinear form. To evaluate the performance of the proposed method, we have optimized the shape of leg-like structural components to minimize compliance during

Table 5: Comparison of the final shape optimization variable values across to the full adaptation study.

Variable	Adaptive Mesh & Sampling	Fine Mesh & Full Sampling
$\mathbb{E}_\xi[J^P]$	0.91	0.37
$\eta^c + \eta^d$	0.04	0.002
$\eta^c$	0.05	0.02
$\eta^d$	0.12	0.04
$ S $	$2 \rightarrow 7$	10
$\alpha_k$	0.008	0.016
$\mathbb{E}_\xi[dJ^P]$	10.57	6.99
$\mathbb{V}_\xi[dJ^P]$	29.05	64.74

Table 6: Comparison of the computational effort between the fixed fine mesh under full sampling and the adaptive mesh and sampling strategy in terms of the degrees of freedom, number of samples, computational runtime, and the computational index defined in (48).

	DoF	$ S_k $	$T_{\text{total}}$ [hours]	CI
fixed	260,282	10	51.0	$397 \cdot 10^9$
adaptive	$29,162 \rightarrow 43,392$	$2 \rightarrow 7$	17.2	$41.9 \cdot 10^9$

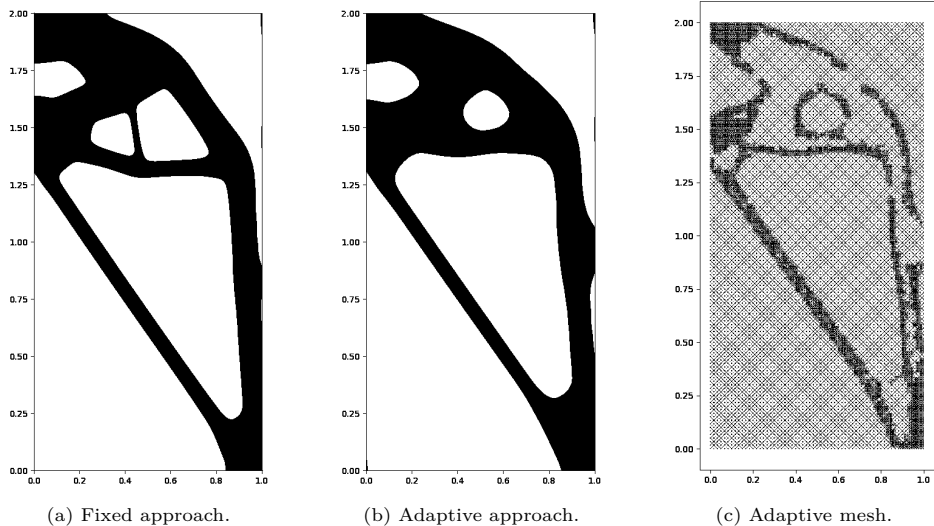


Figure 8: Final optimized designs obtained on a fixed mesh with 260,282 degrees of freedom using full sampling (a) and on an adaptively generated mesh with 43,392 degrees of freedom using adaptive sampling (b). The corresponding adaptive mesh is shown in (c).

touchdown under uncertain contact forces. Numerical experiments demonstrate that the adaptive procedure significantly reduces computational cost while accurately tracking the error behavior, achieving performance comparable to simulations using a fixed fine mesh with full sampling. Future work may focus on reducing the dependence of the final designs on the initial level-set configuration, a behavior noted in our numerical experiments. Possible remedies include adopting a reaction–diffusion–type level-set formulation or enhancing the stability of the Hamilton–Jacobi system by introducing an artificial diffusion term. Moreover, the adaptive framework could be improved by adding a specialized goal functional to better manage discretization errors associated with the Hamilton–Jacobi system.

## Acknowledgements

This work has been supported by Scientific Research Projects Coordination Unit of Middle East Technical University, Ankara, Türkiye under grant number Genel-705-2025-11694. HY also gratefully acknowledges the research support provided by the Scientific and Technological Research Council of Turkey (TUBITAK) through the program 2219–International Postdoctoral Research Fellowship (Project No: 1059B192302207), and would like to thank the Max Planck Institute for Dynamics of Complex Technical Systems, Magdeburg for its excellent hospitality.

## References

- [1] G. Allaire and C. Dapogny. A linearized approach to worst-case design in parametric and geometric shape optimization. *Math. Models Meth. Appl. Sci.*, 24(11):2199–2257, 2014.
- [2] G. Allaire and C. Dapogny. A deterministic approximation method in shape optimization under random uncertainties. *SMAI J. Comput. Math.*, 1:83–143, 2015.
- [3] G. Allaire, F. Jouve, and A.-M. Toader. Structural optimization using sensitivity analysis and a level-set method. *J. Comput. Phys.*, 194(1):363–393, 2004.
- [4] P. R. Amestoy, I. S. Duff, J.-Y. L’Excellent, and J. Koster. A fully asynchronous multifrontal solver using distributed dynamic scheduling. *SIAM J. Matrix Anal. Appl.*, 23(1):15–41, 2001.
- [5] C. Audouze, A. Klein, A. Butscher, N. Morris, P. Nair, and M. Yano. Robust level-set-based topology optimization under uncertainties using anchored ANOVA Petrov–Galerkin method. *SIAM/ASA J. Uncertain. Quantification*, 11(3):877–905, 2023.
- [6] I. Babuška, F. Nobile, and R. Tempone. A stochastic collocation method for elliptic partial differential equations with random input data. *SIAM J. Numer. Anal.*, 45(3):1005–1034, 2007.
- [7] I. Babuška, R. Tempone, and G. E. Zouraris. Galerkin finite element approximations of stochastic elliptic partial differential equations. *SIAM J. Numer. Anal.*, 42(2):800–825, 2004.
- [8] W. Bangerth and R. Rannacher. *Adaptive finite element methods for differential equations*. Lectures in Mathematics ETH Zürich. Birkhäuser Verlag, Basel, 2003.
- [9] N. Banichuk, F.-J. Barthold, A. Falk, and E. Stein. Mesh refinement for shape optimization. *Struct. Optim.*, 9:46–51, 1995.
- [10] R. Becker and R. Rannacher. An optimal control approach to a posteriori error estimation in finite element methods. *Acta Numer.*, 10:1–102, 2001.
- [11] H.-G. Beyer and B. Sendhoff. Robust optimization–A comprehensive survey. *Comput. Methods Appl. Mech. Eng.*, 196(33–34):3190–3218, 2007.

- [12] R. Bollapragada, R. H. Byrd, and J. Nocedal. Adaptive sampling strategies for stochastic optimization. *SIAM J. Optim.*, 28(4):3312–3343, 2018.
- [13] S. C. Brenner and L. R. Scott. *The Mathematical Theory of Finite Element Methods*. Springer, Berlin, third edition, 2008.
- [14] M. Bruggi and M. Verani. A fully adaptive topology optimization algorithm with goal-oriented error control. *Comput. Struct.*, 89(15):1481–1493, 2011.
- [15] R. H. Byrd, G. M. Chin, and J. Nocedal. Sample size selection in optimization methods for machine learning. *Math. Program.*, 134:127–155, 2012.
- [16] C. Cartis and K. Scheinberg. Global convergence rate analysis of unconstrained optimization methods based on probabilistic models. *Math. Program.*, 169:337–375, 2018.
- [17] D. Chenais. On the existence of a solution in a domain identification problem. *J. Math. Anal. Appl.*, 52(2):189–219, 1975.
- [18] D. L. Chopp. Computing minimal surfaces via level set curvature flow. *J. Comput. Phys.*, 106(1):77–91, 1993.
- [19] P. G. Ciarlet. *The Finite Element Method for Elliptic Problems*. North–Holland, Amsterdam, New York, 1978.
- [20] S. Conti, H. Held, M. Pach, M. Rumpf, and R. Schultz. Shape optimization under uncertainty—a stochastic programming perspective. *SIAM J. Optim.*, 19(4):1610–1632, 2009.
- [21] S. Conti, H. Held, M. Pach, M. Rumpf, and R. Schultz. Risk averse shape optimization. *SIAM J. Control Optim.*, 49(3):927–947, 2011.
- [22] M. Dambrine and D. Kateb. On the ersatz material approximation in level-set methods. *ESAIM Control Optim. Calc. Var.*, 16(3):618–634, 2010.
- [23] S. De, J. Hampton, K. Maute, and A. Doostan. Topology optimization under uncertainty using a stochastic gradient-based approach. *Struct. Multidiscip. Optim.*, 62:2255–2278, 2020.
- [24] S. De, K. Maute, and A. Doostan. Bi-fidelity stochastic gradient descent for structural optimization under uncertainty. *Comput. Mech.*, 66(4):745–771, 2020.
- [25] M. C. Delfour and J. P. Zolésio. *Shapes and Geometries: Metrics, Analysis, Differential Calculus, and Optimization*. Society for Industrial and Applied Mathematics (SIAM), 2011.
- [26] N. P. Van Dijk, K. Mauteand M. Langelaar, and F. Van Keulen. Level-set methods for structural topology optimization: a review. *Struct. Multidiscip. Optim.*, 48:437–472, 2013.
- [27] W. Dörfler. A convergent adaptive algorithm for Poisson’s equation. *SIAM J. Numer. Anal.*, 33:1106–1124, 1996.
- [28] B. Endtmayer, U. Langer, T. Richter, A. Schafelner, and T. Wick. Chapter Two - A posteriori single- and multi-goal error control and adaptivity for partial differential equations. In F. Chouly, S. P.A. Bordas, R. Becker, and P. Omnes, editors, *Error Control, Adaptive Discretizations, and Applications, Part 2*, volume 59 of *Advances in Applied Mechanics*, pages 19–108. Elsevier, 2024.
- [29] G. S. Fishman. *Monte Carlo: Concepts, Algorithms, and Applications*. Springer-Verlag, New York, 1996.
- [30] A. Gaathon and A. Degani. Optimizing and designing a leg shape to increase robustness of a running robot on rough terrain. *Bioinspir. Biomim.*, 17(6):066022, 2022.

- [31] C. Geiersbach, E. Loayza-Romero, and K. Welker. Stochastic approximation for optimization in shape spaces. *SIAM J. Optim.*, 31(1):348–376, 2021.
- [32] C. Geiersbach and W. Wollner. A stochastic gradient method with mesh refinement for PDE-constrained optimization under uncertainty. *SIAM J. Sci. Comput.*, 42(5):A2750–A2772, 2020.
- [33] F. De Gournay, G. Allaire, and F. Jouve. Shape and topology optimization of the robust compliance via the level set method. *ESAIM: COCV*, 14(1):43–70, 2008.
- [34] E. Haber, M. Chung, and F. Herrmann. An effective method for parameter estimation with PDE constraints with multiple right-hand side. *SIAM J. Optim.*, 22:739–757, 2012.
- [35] R. Hiptmair, A. Paganini, and S. Sargheini. Comparison of approximate shape gradient. *BIT Numer. Math.*, 55:459–485, 2014.
- [36] L. Jofre and A. Doostan. Rapid aerodynamic shape optimization under uncertainty using a stochastic gradient approach. *Struct. Multidiscip. Optim.*, 65:196, 2022.
- [37] K. Karhunen. Über lineare Methoden in der Wahrscheinlichkeitsrechnung. *Ann. Acad. Sci. Fennicae. Ser. A. I. Math.-Phys.*, 1947(37):79, 1947.
- [38] S. A. Khan, Z. Mehmood, and Z. Afshan. Design, analysis and topology optimization of a landing gear strut for a quadcopter upon impact. In *2021 International Conference on Applied and Engineering Mathematics (ICAEM)*, pages 37–42. IEEE, 2021.
- [39] D. W. Kim and B. M. Kwak. Reliability-based shape optimization of two-dimensional elastic problems using BEM. *Comput. Struct.*, 60(5):743–750, 1996.
- [40] A. Laurain. A level set-based structural optimization code using FEniCS. *Struct. Multidiscip. Optim.*, 58:1311–1334, 2018.
- [41] B. Lazarov, M. Schevenels, and O. Sigmund. Topology optimization considering material and geometric uncertainties using stochastic collocation methods. *Struct. Multidiscip. Optim.*, 46:597–612, 2012.
- [42] M. Loèvre. Fonctions aléatoires de second ordre. *Revue Sci.*, 84:195–206, 1946.
- [43] D. Luft and K. Welker. Computational investigations of an obstacle-type shape optimization problem in the space of smooth shapes. In *Geometric Science of Information: 4th International Conference, GSI 2019, Toulouse, France, August 27–29, 2019, Proceedings 4*, pages 579–588. Springer, 2019.
- [44] M. Martin, S. Krumscheid, and F. Nobile. Complexity analysis of stochastic gradient methods for PDE-constrained optimal control problems with uncertain parameters. *ESAIM Math. Model. Numer. Anal.*, 55(4):1599–1633, 2021.
- [45] J. Martínez-Frutos, D. Herrero-Pérez, M. Kessler, and F. Periago. Robust shape optimization of continuous structures via the level set method. *Comput. Methods Appl. Mech. Eng.*, 305:271–291, 2016.
- [46] P. Morin, R. H. Nochetto, M. S. Pauletti, and M. Verani. Adaptive finite element method for shape optimization. *ESAIM: COCV*, 18(4):1122–1149, 2012.
- [47] K. Noboru, K. Y. Chung, T. Toshikazu, and J. E. Taylor. Adaptive finite element methods for shape optimization of linearly elastic structures. *Comput. Methods Appl. Mech. Eng.*, 57(1):67–89, 1986.
- [48] S. Osher and J. A. Sethian. Fronts propagating with curvature-dependent speed: Algorithms based on Hamilton-Jacobi formulations. *J. Comput. Phys.*, 79(1):12–49, 1988.

- [49] S. Osher and C.-W. Shu. High-order essentially nonoscillatory schemes for Hamilton–Jacobi equations. *SIAM J. Numer. Anal.*, 28(4):907–922, 1991.
- [50] O. Pironneau. *Optimal Shape Design for Elliptic Systems*. Springer-Verlag, New York, Berlin, Heidelberg, Tokyo, 1984.
- [51] A. Schleupen, K. Maute, and E. Ramm. Adaptive FE-procedures in shape optimization. *Struct. Multidiscip. Optim.*, 19:282–302, 2000.
- [52] V. Schulz and M. Siebenborn. Computational comparison of surface metrics for PDE constrained shape optimization. *Comput. Methods Appl. Math.*, 16(3):485–496, 2016.
- [53] R. C. Smith. *Uncertainty Quantification: Theory, Implementation, and Applications*. Society for Industrial and Applied Mathematics, Philadelphia, PA, 2013.
- [54] J. Sokolowski and J.-P. Zolésio. *Introduction to shape optimization*, volume 16 of *Springer Series in Computational Mathematics*. Springer-Verlag, Berlin, 1992.
- [55] K. Sturm. Minimax Lagrangian approach to the differentiability of nonlinear PDE constrained shape functions without saddle point assumption. *SIAM J. Control Optim.*, 53(4):2017–2039, 2015.
- [56] M. Tootkaboni, A. Asadpoure, and J. K. Guest. Topology optimization of continuum structures under uncertainty-A Polynomial Chaos approach. *Comput. Methods Appl. Mech. Eng.*, 201:263–275, 2012.
- [57] S. C. Toraman and H. Yücel. A stochastic gradient algorithm with momentum terms for optimal control problems governed by a convection–diffusion equation with random diffusivity. *J. Comput. Appl. Math.*, 422:114919, 2023.
- [58] M. Y. Wang, X. Wang, and D. Guo. A level set method for structural topology optimization. *Comput. Methods Appl. Mech. Eng.*, 192(1-2):227–246, 2003.
- [59] N. Wiener. The homogeneous chaos. *Amer. J. Math.*, 60:897–938, 1938.
- [60] J. Wong, L. Ryan, and I.Y. Kim. Design optimization of aircraft landing gear assembly under dynamic loading. *Struct. Multidiscip. Optim.*, 57(3):1357–1375, 2018.
- [61] D. Xiu and G. Em Karniadakis. The Wiener–Askey polynomial chaos for stochastic differential equations. *SIAM J. Sci. Comput.*, 24(2):619–644, 2002.